

Geometry and the organizational principle of spine synapses along a dendrite

<https://doi.org/10.1523/ENEURO.0248-20.2020>

Cite as: eNeuro 2020; 10.1523/ENEURO.0248-20.2020

Received: 8 June 2020

Revised: 2 October 2020

Accepted: 7 October 2020

This Early Release article has been peer-reviewed and accepted, but has not been through the composition and copyediting processes. The final version may differ slightly in style or formatting and will contain links to any extended data.

Alerts: Sign up at www.eneuro.org/alerts to receive customized email alerts when the fully formatted version of this article is published.

1 **1. Manuscript Title (11 words):** Geometry and the organizational principle of spine

2 synapses along a dendrite

3 **2. Abbreviated title (46 characters):** Synapse organizational principle in a dendrite

4 **3. Authors name and affiliation:**

5 Laxmi Kumar Parajuli^{1,2}, Hidetoshi Urakubo³, Ai Takahashi-Nakazato¹, Roberto Ogelman⁴,
6 Hirohide Iwasaki^{1,5}, Masato Koike², Hyung-Bae Kwon^{6,7}, Shin Ishii³, Won Chan Oh^{4,6}, Yugo
7 Fukazawa⁸, Shigeo Okabe¹

8 ¹Department of Cellular Neurobiology, Graduate School of Medicine, The University of
9 Tokyo, Tokyo 113-0033, Japan. ²Department of Cell Biology and Neuroscience, Juntendo
10 University Graduate School of Medicine, Tokyo 113-8421, Japan. ³Department of Systems
11 Science, Graduate School of Informatics, Kyoto University, Kyoto 606-8501, Japan.
12 ⁴Department of Pharmacology, University of Colorado School of Medicine, Aurora, CO
13 80045, USA. ⁵ Department of Anatomy, Graduate School of Medicine, Gunma University,
14 Gunma 371-8511, Japan. ⁶ Max Planck Florida Institute for Neuroscience, Jupiter, FL 33458,
15 USA. ⁷ Department of Neuroscience, Johns Hopkins School of Medicine, Baltimore,
16 Maryland 21205, USA. ⁸ Division of Brain Structure and Function, Research Center for Child
17 Mental Development, Life Science Advancement Program, University of Fukui, Fukui 910-
18 1193, Japan.

19 **4. Author contributions:**

20 L.K.P., H.I., M.K., H.B.K., S.I., W.C.O, Y.F., S.O. designed research; L.K.P., H.U., A.T.N.,
21 R.O., W.C.O., Y.F. performed research; L.K.P., H.U., A.T.N., R.O., W.C.O. analyzed data;
22 L.K.P., H.U., W.C.O., Y.F., S.O. wrote the paper.

23 **5. Correspondence should be addressed to:** Dr. Shigeo Okabe; Department of Cellular
24 Neurobiology, Graduate School of Medicine, The University of Tokyo, Tokyo 113-0033,
25 Japan. E-mail : okabe@m.u-tokyo.ac.jp

26 **6. Number of figures:** 6, **7. Number of extended figures:** 7, **8. Number of tables:** 5, **9.**
27 **Number of multimedia:** 0, **10. Number of words for abstract:** 214, **11. Number of words**
28 **for significance statement:** 105, **12. Number of words for introduction:** 619, **13.**
29 **Number of words for discussion:** 1870

30 **14. Acknowledgments:** We thank the members in the Okabe laboratory for helpful
31 discussion. We also thank the Laboratory of Morphology and Image Analysis, Research
32 Support Center, Juntendo University Graduate School of Medicine for technical assistance.

33 **15. Conflict of interest:** The authors report no conflict of interest.

34 **16. Funding sources:** This study was supported by JSPS Grants-in-Aid for Scientific
35 Research (20H00481 to S.O.), Grant-in-Aid for Early-Career Scientists (18K14842 to L.K.P.),
36 the Japan Agency for Medical Research and Development (JP20gm1310003 and
37 JP20gm5010003 to S.O.), and the UTokyo Center for Integrative Science of Human
38 Behavior (CiSHuB) to S.O.

39

40

41

42

43

44

45

46

47

48 **Geometry and the organizational principle of spine synapses**

49 **along a dendrite**

50 **Abstract**

51 Precise information on synapse organization in a dendrite is crucial to understanding
52 the mechanisms underlying voltage integration and the variability in the strength of synaptic
53 inputs across dendrites of different complex morphologies. Here, we used focused ion
54 beam/scanning electron microscope (FIB/SEM) to image the dendritic spines of mice in the
55 hippocampal CA1 region, CA3 region, somatosensory cortex, striatum, and cerebellum (CB).
56 Our results show that the spine geometry and dimensions differ across neuronal cell types.
57 Despite this difference, dendritic spines were organized in an orchestrated manner such that
58 the postsynaptic density (PSD) area per unit length of dendrite scaled positively with the
59 dendritic diameter in CA1 proximal stratum radiatum (PSR), cortex and CB. The ratio of the
60 PSD area to neck length was kept relatively uniform across dendrites of different diameters
61 in CA1 PSR. Computer simulation suggests that a similar level of synaptic strength across
62 different dendrites in CA1 PSR enables the effective transfer of synaptic inputs from the
63 dendrites towards soma. Excitatory postsynaptic potentials (EPSPs), evoked at single spines
64 by glutamate uncaging and recorded at the soma, show that the neck length is more
65 influential than head width in regulating the EPSP magnitude at the soma. Our study
66 describes thorough morphological features and the organizational principles of dendritic
67 spines in different brain regions.

68

69 **Keywords:** Dendritic spine, Electron microscopy, FIB/SEM, Glutamate uncaging,
70 Postsynaptic density, Simulation

71

72 **Significance statement**

73 Little is known about the characteristic anatomical features underlying the
74 organization of spine synapses in a dendrite. This study used volume electron microscopy to
75 make an extensive characterization of dendritic spine synapses in multiple regions of the
76 mouse brain to uncover the principles underlying their placement along a dendritic shaft. By
77 using a combination of approaches such as two-photon imaging, glutamate uncaging,
78 electrophysiology, and computer simulation, we reveal the functional importance of regulated
79 spine placement along a dendritic trunk. Our research presents a crucial step in
80 understanding the synaptic computational principle in dendrites by highlighting the
81 generalizable features of dendritic spine organization in a neuron.

82

83

84

85

86

87

88

89

90

91

92

93 **Introduction**

94 Neurons communicate with each other via synapses. In multiple brain regions,
95 synaptic communications occur through tiny dendritic protrusions called dendritic spines
96 (Parajuli et al., 2017). Evidence suggests that the placement of synapses in a dendrite
97 occurs in a regulated manner (Jones and Powell, 1969; Magee and Cook, 2000; Konur et al.,
98 2003, Katz et al., 2009; Menon et al., 2013; Walker et al., 2017). The plastic nature of
99 dendritic spines (Matsuzaki et al., 2004) and their ability to cross-talk with each other (Royer
100 and Paré, 2003; Oh et al., 2015) hint at the possibility that dendritic spines are organized to
101 maintain a set of optimal rules.

102 Neurons from different brain regions are distinct in terms of the gross anatomical
103 features. In addition, a single neuron shows considerable variability in the size and shape of
104 dendritic arbors (Harris and Spacek, 2016; Parajuli et al., 2020a), thereby creating variation
105 in the electrical properties among different dendritic compartments. Thus, defining the spatial
106 organizational principle of synapses in a dendrite is key to understanding how the
107 mechanism of voltage integration differs along the somatodendritic arbor in diverse neurites.
108 Furthermore, there has recently been an enormous surge of interest in mapping each of the
109 neuronal connections in the brain (Bock et al., 2011; Kasthuri et al., 2015; Markram et al.,
110 2015). However, even with the latest automated large-scale electron microscopic (EM)
111 techniques, it is impractical to achieve comprehensive sorting of individual neuron-to-neuron
112 connections. Thus, in recent years investigators feel the urge to minimize the effort and cost
113 involved in connectomics studies by studying a handful of brain regions and extracting some
114 common organizational principles for neuronal connections in those regions. Decoding
115 principles of synapse placement in a handful of brain regions might eventually aid in
116 formulating a set of algorithms that apply to most brain nuclei.

117 Studies in the past have used conventional transmission electron microscopy (TEM)
118 to make both qualitative and quantitative descriptions of dendritic spines (Wilson et al., 1983;
119 Harris and Stevens, 1988, 1989; Harris et al., 1992; Schikorski and Stevens, 1997). Several
120 past studies are limited to single section observations. Even with the approach of serial
121 sectioning, imaging volume is often small because the manual collection and image
122 acquisition of hundreds of thin sections is technically demanding. Most of the previous
123 studies did not attempt to study spines in relation to their parent dendrites. A survey of the
124 spine position along the dendritic arbor can reveal how synaptic conductance scales up to
125 counterbalance the effect of passive membrane properties in dendrites (Rall, 1962; Katz et
126 al., 2009). Furthermore, no studies have yet been undertaken to compare and contrast the
127 synapse structure between different brain regions and decipher which principles are
128 universal and which aspects are intrinsic to a given brain region. It is not directly possible to
129 compare the findings from different studies as there are inconsistencies in the results due to
130 differences in the genetic background of animal models, sample preparation, and analysis
131 methods.

132 Since synaptic junctions are too small to be resolved by light microscopy (Okabe,
133 2020), here we used focused ion beam/scanning electron microscope (FIB/SEM) to perform
134 automatic imaging of neuropils from multiple brain regions that exhibit numerous dendritic
135 spines. By large volume reconstruction at the synaptic level resolution, we construct a
136 quantitative description of the morphological features of dendritic shafts, dendritic spines,
137 and their presynaptic connectivity pattern, and reveal the principle defining dendritic spine
138 organization in a dendrite. Using two-photon glutamate uncaging and electrophysiological
139 recording, we show that the spine neck length is more influential than head width in
140 regulating the magnitude of excitatory postsynaptic potentials (EPSPs) at the soma. In
141 summary, we report the organizational principle of dendritic spine synapses in their parent
142 dendrites across multiple brain regions.

143

144

145

146

147 **Materials and Methods**

148 **Electron microscopy**

149 **Animals**

150 A total of four C57BL/6 male mice at 12 weeks of age were used for this study. All
151 the animals were raised in a standard light-dark cycle and had free access to food and water.
152 The animal handling protocol was approved by the animal care and use committee of the
153 authors' institutions. Mouse housing and euthanization strictly adhered to the guidelines
154 provided by the government and the university. Efforts were made to reduce the pain and
155 suffering of the animals used in the experiment.

156

157 **Tissue preparation for FIB/SEM analysis**

158 Sample preparation for FIB/SEM was performed as described previously (Takahashi-
159 Nakazato et al., 2019). Mice were anesthetized by intraperitoneal injection of somnopentyl
160 (10 ml/kg body weight) and transcardially perfused with 20 ml of Ringer's solution, followed
161 by 70 ml of 2% paraformaldehyde and 2.5% glutaraldehyde made up in 0.1 M cacodylate
162 buffer (pH 7.4). The brains were quickly removed and postfixed for 1 h at room temperature
163 in 4% paraformaldehyde solution. After several washes in cacodylate buffer, 100 μ m thick
164 sections were cut in ice-cold 0.1 M phosphate buffer (pH 7.4, PB) using a vibratome (Leica
165 VT 1000S). Sections were washed in cacodylate buffer containing 2 mM calcium chloride.
166 Sections were then incubated in a freshly prepared solution containing 3% potassium
167 ferrocyanide (made up in 0.2 M cacodylate buffer and supplemented with 4 mM calcium
168 chloride) combined with an equal volume of 4% aqueous osmium tetroxide. Sections were

169 then washed in Milli-Q water (Millipore) and incubated at room temperature for 20 min in the
170 thiocarbohydrazide solution. The solution was prepared by incubating 0.1 g of
171 thiocarbohydrazide in 10 ml ddH₂O in a 60°C oven for 1 h. The sections were then placed in
172 a 2% aqueous osmium tetroxide solution for 30 min, washed briefly, and incubated overnight
173 in 1% uranyl acetate. The sections were further stained with filtered Walton's lead aspartate
174 solution in a 60°C oven for 75 min and then dehydrated in ascending series of ethanol.
175 Slices were placed in propylene oxide solution, gradually equilibrated with Durcupan resin,
176 flat embedded, and placed in a 60°C oven for 48 h for resin curing and polymerization.

177

178 **FIB/SEM imaging**

179 Resin blocks containing the section of interest were mounted on metal stubs. The
180 block was trimmed with a diamond knife to expose the resin tissue interface to the surface.
181 We prevent specimen charging by painting the stub with graphene at block sides, and
182 coating with a 5-7 nm-thick carbon layer over block faces using a BAF060 freeze-fracture
183 replica machine (Leica). Aluminum stubs containing the specimen were placed in the
184 FIB/SEM stage (FEI), and images were acquired at an acceleration voltage of 1.4 kV, dwell
185 time: 5 μs and z-step: 40 nm. Images were taken at 17500× magnification, covering a
186 horizontal field width of 11.84 μm at a resolution of 3072 × 2048 pixels. Automated
187 acquisition of 200-450 serial images was performed by the sequential repetition of sample
188 milling and imaging using Auto Slice and View G3 software (FEI).

189 FIB/SEM images were acquired from the proximal stratum radiatum (PSR) and
190 stratum lacunosum-moleculare (SLM) of hippocampal CA1, PSR of hippocampal CA3, layer
191 1 of the somatosensory cortex, striatum and molecular layer of the cerebellum (CB).

192

193 **Three-Dimensional reconstruction and quantitative analysis of neuropil from**

194 **FIB/SEM images**

195 Images were first aligned with the aid of Fiji software (Schindelin et al., 2012) and
196 then loaded onto Reconstruct software (Fiala, 2005) for manual segmentation of the
197 neuronal profiles of interest. Volume reconstruction and measurement of the profile
198 dimensions were performed using Reconstruct. Only a complete spine whose head and
199 neck were contained within the imaging volume was analyzed. The spine head volume was
200 obtained by multiplying the total cross-sectional area of the plasma membrane contours with
201 the section thickness. Postsynaptic density (PSD) area in a cross-sectioned synapse was
202 calculated by multiplying section thickness with the summed length of PSD in consecutive
203 sections. For synapses cut *en face*, the PSD area was obtained in the single section.
204 Dendritic length, neck length, and neck diameter were measured in 3D reconstructed images
205 in reference to the $1\ \mu\text{m}^3$ scale cube. The dendritic diameter was obtained by computing the
206 average length of the line that was drawn across the widest transect of the narrowest
207 dimension of the ovoid profile. Spine density was obtained by dividing the number of spines
208 in a dendrite by the length of the reconstructed dendrite. PSD area density (expressed as
209 the PSD area per unit length of the dendrite) was obtained by dividing the summed PSD
210 area of all the spines in a dendritic segment by the length of the dendrite. Occasionally,
211 some spine necks extended beyond the field of view, and this prevented us from measuring
212 the PSD area in that spine. Thorny excrescence spines in CA3 were only used as an
213 example to show their vast difference in spine morphology from that of typical spines in other
214 brain regions. We did not perform any quantification of the synaptic density and neck length
215 from CA3 thorny excrescence spines. In the CB, quantitative analysis was exclusively
216 performed from Purkinje cell spines that made synaptic contacts with the parallel fiber
217 terminals. Climbing fiber–Purkinje cell synapses were rarely observed in our FIB/SEM
218 images.

219

220 **Pre-embedding immunogold labeling**

221 Pre-embedding immunogold labeling was carried out as described in Parajuli et al.
 222 (2020b). We perfused a mouse with 75 ml of fixative containing 4% PFA and 0.05%
 223 glutaraldehyde. Fifty-micrometer cryoprotected sections were freeze-thawed and incubated
 224 in a blocking solution containing 20% normal goat serum in 50 mM Tris-buffered saline.
 225 Sections were incubated for 48 h with 1 μ g/ml of Inositol 1,4,5-trisphosphate receptor type 1
 226 (IP₃R1) antibody (Frontier Institute) and then overnight in 1.4 nm gold conjugated anti-rabbit
 227 secondary antibody (Nanoprobes). Immunoreactivity was visualized by placing sections in
 228 the HQ silver intensification solution (Nanoprobes). Sections were osmicated for 40 min,
 229 followed by incubation in 1% uranyl acetate for 35 min at room temperature. Sections were
 230 dehydrated in graded ethanol series of 50%, 70%, 80%, 90%, and 100% for 10 min each
 231 and incubated for another 10 min in propylene oxide to facilitate resin penetration. Sections
 232 were placed in freshly prepared resin overnight for resin infiltration and placed in a 60°C
 233 oven for 48 h for resin curing. Seventy-nanometer ultrathin sections were cut with a Leica
 234 Ultracut UCT microtome and collected on formvar-coated single-slot grids. After that, they
 235 were counterstained using Reynold's lead citrate and imaged using a JEM-1010 TEM
 236 (JEOL). Single section images were randomly acquired from the cortex, striatum, and CB,
 237 and the frequency of immunogold positive spine profiles in each brain region was counted.

238

239 **Two-photon imaging, glutamate uncaging and electrophysiology**

240 **Preparation of hippocampal slices.**

241 Acute coronal hippocampal slices were prepared from C57BL/6 wild type mice, P30 -
 242 43. Mice were anesthetized with isoflurane and decapitated. The brain was removed from
 243 the skull and rapidly placed in an ice-cold cutting solution containing (in mM): 215 sucrose,
 244 20 glucose, 26 NaHCO₃, 4 MgCl₂, 4 MgSO₄, 1.6 NaH₂PO₄, 1 CaCl₂, and 2.5 KCl. Coronal
 245 slices (300 μ m thick) were prepared using a VT1000S vibrating microtome (Leica). Slices
 246 were incubated at 32°C for 30 minutes in a holding chamber containing 50% cutting solution

247 and 50% artificial cerebrospinal fluid (ACSF; in mM: 127 NaCl, 25 NaHCO₃, 1.25 NaH₂PO₄,
 248 2.5 KCl, 25 D-glucose, 2 CaCl₂, and 1 MgCl₂). After 30 min, this solution was replaced with
 249 ACSF at room temperature. Slices were allowed to recover for more than 1 h in ACSF
 250 before imaging and recording. All solutions were equilibrated for at least 30 min with
 251 95%O₂/5%CO₂. Organotypic hippocampal slice cultures were prepared from postnatal day 3
 252 (P3) mice, following the guidelines set by the institutional animal care and use committee at
 253 the authors' institution.

254 **Two-photon imaging, uncaging and electrophysiology**

255 CA1 pyramidal neurons were imaged using a two-photon microscope (Prairie
 256 Technologies, Inc) with a pulsed Ti:sapphire laser (MaiTai HP DeepSee, Spectra-Physics)
 257 tuned to 920 nm (3-4 mW at the sample) in recirculating ACSF aerated with 95%O₂/5%CO₂
 258 containing (in mM): 0.001 TTX, and 2.3-2.5 MNI-caged-glutamate. For each neuron, image
 259 stacks (512 × 512 pixels; 0.035 μm / pixel) with 1 μm z-steps were collected from several
 260 secondary or tertiary apical and/or basal dendrites (average of three dendrites per cell)
 261 located 40-80 μm from the soma. All images shown are maximum projections of 3D image
 262 stacks after applying a median filter (2 × 2) to the raw image data. Uncaging of MNI-
 263 glutamate was achieved as described (Oh et al., 2016). In brief, whole-cell recordings
 264 (electrode resistance 6-8 MΩ; series resistance 20-40 MΩ) were performed at 30°C on
 265 visually identified CA1 pyramidal neurons using a MultiClamp 700B amplifier (Molecular
 266 Devices). In order to record uncaging-evoked excitatory postsynaptic currents (uEPSCs),
 267 CA1 pyramidal neurons of acute hippocampal slices at depths of 20-40 μm were patched in
 268 voltage-clamp configuration ($V_{\text{hold}} = -65$ mV for AMPA receptor-mediated uEPSCs) using
 269 cesium-based internal solution (in mM: 135 Cs-methanesulfonate, 10 HEPES, 10 Na₂-
 270 phosphocreatine, 4 MgCl₂, 4 Na₂-ATP, 0.4 Na-GTP, 3 Na L-ascorbate, 0.2 Alexa 488; ~300
 271 mOsm, ~pH 7.25) in ACSF. Uncaging-evoked excitatory postsynaptic potentials (uEPSPs)
 272 were measured from 28 days *in vitro* (DIV) CA1 pyramidal neurons of organotypic slice
 273 cultures in current-clamp configuration ($I = 0$) using potassium-based internal solution (in

274 mM: 136 K-gluconate, 10 HEPES, 17.5 KCl, 9 NaCl, 1 MgCl₂, 4 Na₂-ATP, 0.4 Na-GTP;
 275 ~300 mOsm, ~pH 7.26) at 30°C in ACSF containing 2 mM Ca²⁺ and 1 mM Mg²⁺. uEPSPs
 276 were recorded from individual spines with different neck lengths and head sizes. uEPSC or
 277 uEPSP amplitudes from several spines (average of four spines per dendrite) that were well
 278 isolated from each other on a single dendritic segment were quantified as the average (5-10
 279 test pulses of 2 ms duration at 0.1 Hz) from a 2 ms window centered on the maximum
 280 current amplitude after uncaging pulse delivery. Laser pulses were delivered by parking the
 281 beam at a point ~0.5 μm from the center of the spine head with a pulsed Ti:sapphire laser
 282 (MaiTai HP, Spectra-Physics) tuned to 720 nm (17-20 mW at the sample).

283

284 **Quantification of fluorescence intensities of dendritic spines**

285 Integrated green fluorescence intensities were measured from background-
 286 subtracted green fluorescence (Alexa 488 in internal solution) using the integrated pixel
 287 intensity of a boxed region surrounding the spine head. The estimated spine size was
 288 calculated by normalizing the fluorescence intensities for each spine on a single dendritic
 289 segment to the mean fluorescence intensities measured from four regions of interest (ROIs)
 290 on the dendritic shaft. Spine length/spine width ratio was obtained by dividing the spine
 291 length (measured from the tip of the spine head to the base of the spine neck) by the spine
 292 head width at its widest transect (Woods et al., 2011). For spines that show no discernible
 293 necks, we set a minimum length of 0.2 μm, as previously described (Araya et al., 2006b,
 294 2014).

295

296 **Computer simulation study**

297 **Two-layer model neuron**

298 We developed a two-layer model neuron that consists of 20 branches ($N_{branch} = 20$)
 299 with each branch having 250 synapses ($N_{syn} = 250$). If each synapse i at the branch j follows

300 an input sequence $\{t_{i,j,1}, t_{i,j,2}, \dots, t_{i,j,k}\}$, the total synaptic input to the branch $I_j(t)$ can be
 301 described by:

$$I_j(t) = \sum_i^{N_{syn}} \sum_k W_{i,j} \delta(t - t_{i,j,k}),$$

302 Where $W_{i,j}$ is the synaptic weight, and $\delta(t)$ is the Dirac's delta function. Here, the input
 303 sequence $\{t_{i,j,1}, t_{i,j,2}, \dots, t_{i,j,k}\}$ obeys a Poisson process with the input frequency ranging from
 304 0.5 Hz to 10 Hz. The synaptic weight $W_{i,j}$ was sampled from the lognormal distribution:

$$P_W(X) = \frac{1}{\sqrt{2\pi}\sigma_e X} \exp\left(-\frac{(\log X - \mu_e)^2}{2\sigma_e^2}\right),$$

305 where μ_e and σ_e respectively represent the location and shape parameters of the probability
 306 distribution. Dendritic membrane potential V_j depolarized by the summed synaptic input $I_j(t)$
 307 results in the occurrence of dendritic spikes as:

$$\frac{dV_j}{dt} = -\frac{(V_j - V_{rest})}{\tau_{dend}} + I_j(t),$$

308 if $V_j > \theta$, then $V \rightarrow V_{reset,dend}$,

309 where V_{rest} represents the resting membrane potential, $V_{reset,dend}$ represents the dendritic
 310 reset potential, τ_{dend} represents the dendritic membrane time constant, and θ represents the
 311 spiking threshold. In our simulation, we set V_{rest} and $V_{reset,dend}$ to -75 mV, τ_{dend} to 10 ms, and
 312 θ to -40 mV. A relative refractory period of 20 ms was imposed on the dendritic spikes that
 313 occur in the model dendritic branches.

314 Dendritic spike mediated depolarization of somatic membrane potential V_m and firing
 315 of a somatic spike is expressed as:

$$\frac{dV_m}{dt} = -\frac{(V_m - V_{rest})}{\tau_{soma}} + \sum_i^{N_{branch}} \sum_j W \delta(t - t_{i,j}^{dend}),$$

316 if $V_m > \theta$, then $V_m \rightarrow V_{reset,soma}$,

317 where $\{t_{i,1}^{dend}, t_{i,2}^{dend}, \dots, t_{i,j}^{dend}\}$ is the dendritic spike sequence from the branch i , W is the
 318 weight (the level of synaptic depolarization by a dendritic spike), $V_{reset,soma}$ is the somatic
 319 reset potential, and τ_{soma} is the somatic membrane time constant. We set W to 20 mV, τ_{soma}
 320 to 20 ms, and $V_{reset,soma}$ to -80 mV. The model soma had a relative refractory period of 20 ms.
 321 τ_{soma} and τ_{dend} were determined based on a previous study (Routh et al., 2009). The output
 322 somatic spike sequences $\{t_1^{soma}, t_2^{soma}, \dots, t_i^{soma}\}$ were subjected to further analysis.

323

324

325

326 **Mutual information**

327 First, we targeted the input sequence to the strongest synapse, $imax$, at each branch,
 328 j , $\{t_{imax,j,1}, t_{imax,j,2}, \dots, t_{imax,j,k}\}$. The input sequence was binned to 5 ms intervals and binarized
 329 (Synaptic input (SI) = 0 for the absence of synaptic input; SI = 1, for the occurrence for input).
 330 Information transfer by the occurrence of dendritic spikes $\{t_{i,1}^{dend}, t_{i,2}^{dend}, \dots, t_{i,j}^{dend}\}$ within the
 331 same time bins (Dendritic spike (DS) = 0 for the absence of dendritic spike; DS = 1 for the
 332 occurrence of dendritic spike) were quantified using mutual information (MI) :

$$MI(DS; SI) = \sum_{DS \in \{0,1\}} \sum_{SI \in \{0,1\}} p(DS, SI) \log \frac{p(DS, SI)}{p(DS)p(SI)}$$

333 We also measured the MI between the strongest synaptic input sequence and
 334 somatic spike sequence, i.e., MI (SS ; SI), where SS represents the occurrence of somatic
 335 spikes within the same time bins (Somatic spike (SS) = 0 for the absence of somatic spike;
 336 SS = 1 for the occurrence of somatic spike).

337

338 **Code Accessibility**

339 Computer simulation was carried out using MATLAB (R2019a, MathWorks Inc.). The
340 MATLAB code that we have generated in this study is freely available online at the public
341 repository GitHub (<https://github.com/urakubo/Parajuli>).

342

343 **Statistics**

344 Statistical tests were performed using IBM SPSS statistics software (IBM, version 24).
345 The normality of the data sets was examined by Shapiro–Wilk test. Student’s *t*-test
346 compared statistical significance between two populations for parametric data sets and
347 Mann–Whitney *U* test for data that are distributed in a non-parametric manner. Either one-
348 way ANOVA or the Kruskal–Wallis test was used to examine statistical significance between
349 three or more groups. The correlation was analyzed by Pearson’s correlation or Spearman’s
350 rank order test, as appropriate. Unless otherwise mentioned, data are expressed as mean \pm
351 standard deviation (SD). The number of profiles analyzed for statistical analysis is provided
352 in the table. Statistical significance was set at $p = 0.05$. Single, double and triple asterisks in
353 the figures and tables denote *p*-values less than 0.05, 0.01, and 0.001, respectively. Where
354 appropriate, the correlation coefficient and the statistical significance values in the graphs
355 are denoted by *r* and *p*, respectively.

356

357 RESULTS

358 Ultrastructure of dendritic spines in multiple brain regions

359 High quality, well-preserved morphology is a prerequisite for ultrastructural studies. In
360 our sample, we could visualize plasma membranes, synaptic contacts, and PSDs at a fine
361 level of detail and could resolve the fine morphology of organelles such as mitochondria and
362 endoplasmic reticulum (ER) (Fig. 1A, B). The high-quality images aided unequivocal
363 segmentation of membrane contours. We reconstructed 5-25 μm long dendrites (C-H) by
364 manual segmentation of 150-450 consecutive FIB/SEM images. A total of 86 dendrites and
365 2078 spines were reconstructed from six different brain regions (CA1 PSR, CA1 SLM, CA3
366 PSR, layer 1 of the somatosensory cortex, dorsolateral striatum and the molecular layer of
367 CB). The imaging volume in CA1 PSR and CB were located at a distance of $\sim 100 \mu\text{m}$ from
368 the edge of the CA1 pyramidal cell layer and Purkinje cell layer, respectively.

369 Spines of various morphologies were seen protruding from the same parent dendrite.
370 Typically, spines had a narrow neck and bulbous head. However, such a feature was not
371 always apparent, and in some spines, the segregation of head and neck relied upon the
372 subjective judgment of the annotator. Thorny excrescence spines in CA3 (Fig. 1R) were
373 distinct from the spines in other brain regions as they were unusually large and contained
374 several mitochondria in the spine head. Several spines in CB (Fig. 1Q) had a ladle-shaped
375 morphology such that the spine head was tilted roughly at an angle of 60° relative to the
376 spine neck. However, in CA1 PSR, CA1 SLM, cortex, and striatum, both the spine head and
377 spine neck often resided in the same plane (Fig. 1I-P). Almost all the spiny protrusions
378 displayed synaptic contacts with their presynaptic partners (Table 1). In the case of CA1
379 PSR, CA1 SLM, cortex, and striatum, the synaptic contact was mostly located at the tip of
380 the spine head (Fig. 1I-P), but it could reside in any part of the spine head in CB (Fig. 1Q).
381 PSD in CB was always of macular type, whereas in CA1 SLM, half of the spines had
382 perforated PSD. Less than 10% of the spines in other brain regions had perforated PSD

(Table 1). While the spine necks in CA1, cortex, and CB appeared to be cylindrical with roughly similar diameter throughout the length of the dendrite, striatal spine necks occasionally displayed widening roughly at the midway (Fig. 1N). Approximately 10% of the spines were branched in CA1 PSR, cortex, striatum, and CB (Table 1). Sometimes filopodia-like protrusions also branched out from the necks of spines (Fig. 1M). Interestingly, we did not encounter any branched spines in CA1 SLM. The proportion surface area occupied by the dendritic shaft, spine head, PSD, and spine neck also varied depending on the brain regions (Fig. 1S).

Next, we analyzed if each brain region contained spines of distinct dimensions (Fig. 2A- C). The mean values for the head volume, neck length, and neck diameter in each brain region are shown in Table 2. The average spine head volumes (in μm^3) were 0.05 ± 0.045 in CA1 PSR, 0.12 ± 0.086 in CA1 SLM, 0.08 ± 0.101 in cortex, 0.07 ± 0.109 in striatum and 0.13 ± 0.035 in CB. The distribution of head volume was not significantly different between the spines in CA1 PSR and striatum ($p = 1.00$, Kruskal–Wallis test with Bonferroni correction). However, except for this pair, statistical significance could be detected when spine head volume was compared between any of the two regions studied here (p -values between CA1 PSR and CA1 SLM < 0.001 , CA1 PSR and cortex < 0.01 , CA1 PSR and CB < 0.001 , CA1 SLM and cortex < 0.001 , CA1 SLM and striatum < 0.001 , CA1 SLM and CB $= 0.03$, cortex and striatum $= 0.01$, cortex and CB < 0.001 , striatum and CB < 0.001 , Kruskal–Wallis test with Bonferroni correction). Despite the significant differences in the spine head volume, spines from different regions of the brain were not readily distinguishable from each other because of the significant overlap in their head dimensions (Fig. 2A). There was a 124 to 204-fold difference in the head volume dimensions between the smallest and the largest spines in CA1 PSR, cortex, and striatum. Relatively smaller variation was observed in CA1 SLM (35-fold) and CB (11-fold).

Spine neck dimensions also differed among brain areas (Fig. 2B). Despite the significant differences in the distribution of spine head volume, statistical significance was

not revealed in the distribution of neck lengths between the spines in CA1 PSR and CA1 SLM, and between the spines in cortex and striatum (average neck lengths (in μm) in CA1 PSR = 0.46 ± 0.246 , CA1 SLM = 0.49 ± 0.289 , cortex = 1.09 ± 0.561 , striatum = 1.12 ± 0.556 , CB = 0.74 ± 0.300 ; p -values between CA1 PSR and CA1 SLM = 1.00, cortex and striatum = 1.00, Kruskal–Wallis test with Bonferroni correction). Except for these pairs, all other brain regions showed statistical significance in the distribution of spine neck length (p -values between CA1 PSR and cortex < 0.001, CA1 PSR and striatum < 0.001, CA1 PSR and CB < 0.001, CA1 SLM and cortex < 0.001, CA1 SLM and striatum < 0.001, CA1 SLM and CB < 0.001, cortex and CB < 0.001, striatum and CB < 0.001; Kruskal–Wallis test with Bonferroni correction). Similar to the large variability observed in the head volume, the ratio of neck lengths of the longest to the shortest necks also varied by several fold (fold differences: CA1 PSR = 38, CA1 SLM = 15, cortex = 20, striatum = 106, CB = 27; Table 2).

Next, we tested if the brain regions with longer spine necks also showed the tendency to have spines with wide necks. However, we found that the spine neck length is a poor predictor of the spine neck diameter (Fig. 2C, Table 2). In particular, spines in cortex and striatum had longer necks than the spines in other brain regions. However, cortex and striatum neither had the widest, nor the narrowest, neck diameter (average neck diameter (in μm) in CA1 PSR = 0.20 ± 0.087 , CA1 SLM = 0.25 ± 0.127 , cortex = 0.23 ± 0.121 , striatum = 0.26 ± 0.104 , CB = 0.27 ± 0.054). Cortical and striatal spines had significantly thicker necks than the spines in CA1 PSR and significantly thinner necks than the spines in CB (p -values between CA1 PSR and cortex < 0.01, CA1 PSR and striatum < 0.001, cortex and CB < 0.001, striatum and CB < 0.001, Kruskal–Wallis test with Bonferroni correction). Spine neck diameter in CA1 PSR was significantly smaller than in the CB (p -value between CA1 PSR and CB < 0.001, Kruskal–Wallis test with Bonferroni correction). The distribution of spine neck diameter in cortex and striatum was not significantly different from the spines in CA1 SLM (p -values between CA1 SLM and cortex = 1.00, CA1 SLM and striatum = 1.00, Kruskal–Wallis test with Bonferroni correction). In contrast, CA1 SLM spines had significantly

437 wider necks compared to CA1 PSR and significantly narrower neck compared to CB (p -
 438 values between CA1 SLM and CA1 PSR < 0.01 , CA1 SLM and CB < 0.001 , Kruskal–Wallis
 439 test with Bonferroni correction). Interestingly, despite the similarity in the neck lengths, a
 440 significant difference in neck diameter was observed between the spines in cortex and
 441 striatum (p -value between cortex and striatum < 0.01 , Kruskal–Wallis test with Bonferroni
 442 correction).

443 The magnitude of EPSPs at the soma, generated by the activation of a dendritic
 444 spine, is critically influenced by the dimensions of the spine head volume and the neck
 445 length (Matsuzaki et al., 2001; Araya et al., 2006b, 2014). The spine head volume is
 446 positively correlated with the PSD area (CA1 PSR, $r = 0.80$, $p < 0.001$; CA1 SLM, $r = 0.89$, p
 447 < 0.001 ; cortex, $r = 0.86$, $p < 0.001$; striatum, $r = 0.80$, $p < 0.001$; CB, $r = 0.42$, $p < 0.001$;
 448 Spearman's rank order test; Fig. 2-1A-E) and, in turn, the PSD area positively correlates with
 449 the AMPA receptor content (Nusser et al., 1998). This suggests that the size of the spine
 450 head is an important parameter that determines the magnitude of synaptic strength. Indeed,
 451 using two-photon microscopy, glutamate uncaging and electrophysiological recordings in
 452 hippocampal CA1 pyramidal neurons, we revealed that the magnitude of uEPSC recorded at
 453 the soma is positively correlated with the head volume of the activated spines (Fig. 2-2). In
 454 contrast to the role of spine head in somatic membrane depolarization, spine necks
 455 attenuate membrane potentials (Araya et al., 2006b, 2014; also Fig. 4 and Fig. 4-1 in this
 456 study). Thus, larger spine heads (i.e., larger PSD areas) and shorter spine necks generate
 457 stronger membrane depolarization at the soma than the spines with smaller heads and
 458 longer necks. Simply put, the synaptic strength of a spine can be expressed by the ratio of
 459 the spine head volume (or the PSD area) to the spine neck length. Interestingly, despite the
 460 large differences in the average head volume and the average neck length of spines
 461 between CA1 PSR and CB, we found that the ratio of PSD area to neck length was similar
 462 between these two regions (CA1 PSR: 0.19 ± 0.193 , CB: 0.17 ± 0.130 ; $p = 1.00$, Kruskal–
 463 Wallis test with Bonferroni correction, Fig. 2D). However, the spines in other brain regions

464 were significantly different in terms of the ratio of the PSD area to the neck length (CA1
 465 SLM: 0.32 ± 0.323 , cortex: 0.13 ± 0.169 , striatum: 0.11 ± 0.204 ; p -values between CA1 PSR
 466 and CA1 SLM < 0.01 , CA1 PSR and cortex < 0.001 , CA1 PSR and striatum < 0.001 , CA1
 467 SLM and cortex < 0.001 , CA1 SLM and striatum < 0.001 , CA1 SLM and CB = 0.01, cortex
 468 and striatum < 0.01 , cortex and CB < 0.001 , striatum and CB < 0.001 ; Kruskal–Wallis test
 469 with Bonferroni correction, Fig. 2D). Head volume and neck length are likely to be
 470 independently regulated as either no correlation or only a weak, but statistically significant,
 471 correlation was observed between these two parameters (CA1 PSR: $r = 0.02$, $p = 0.63$; CA1
 472 SLM: $r = -0.11$, $p = 0.38$; cortex: $r = -0.12$, $p = 0.08$; striatum: $r = -0.27$, $p < 0.001$; CB: $r = -$
 473 0.15 , $p < 0.001$; Spearman's rank order test; Fig. 2-1F-J).

474 After having obtained the precise measurement of the spine head volume, spine
 475 neck length, and spine neck diameter, we asked if the combination of these structural
 476 features of spines would enable us to identify the brain region where the spines were
 477 sampled. The average neck length, average PSD area, and average neck diameter of
 478 spines was obtained from each dendrite and plotted in x, y, and z-axes. Since it is not
 479 possible to segregate individual spines from different brain regions due to large variability in
 480 their dimensions (Fig. 2A, B, C), we wondered whether averaging the dimensions of spines
 481 in each dendrite would make it possible to identify the region that a dendrite is sampled from.
 482 However, a three-dimensional scatter plot revealed that the dendrites from different brain
 483 regions show a considerable overlap in the average spine dimensions (Fig. 2E). We
 484 conclude that based on the combination of average neck length, average PSD area, and
 485 average neck diameter, it is not possible to unequivocally identify the sampled brain region.

486 The relative abundance of dendritic spines differs between the brain regions (Fig. 2F).
 487 We calculated the density of spines in individual dendrites by dividing the total number of
 488 spines by the length of the dendrite. The Purkinje cell dendrites had the highest density of
 489 spines, followed by the dendrites in CA1 PSR and striatum (spine density (spines/ μm) in CB
 490 $= 7.10 \pm 1.693$, CA1 PSR $= 3.04 \pm 0.825$, striatum $= 1.94 \pm 0.621$). Dendritic spines were

491 sparse in the dendrites of CA1 SLM and cortex (spine density (spines/ μm) in CA1 SLM =
 492 0.75 ± 0.360 , cortex = 1.14 ± 0.723) and the spine density was not significantly different
 493 between these two regions ($p = 0.45$, one-way ANOVA). However, except for this pair, the
 494 difference in spine density was statistically significant between any of the two regions
 495 studied here (p -values between CA1 PSR and CA1 SLM < 0.001 , CA1 PSR and cortex $<$
 496 0.001 , CA1 PSR and striatum < 0.01 , CA1 PSR and CB < 0.001 , CA1 SLM and striatum $<$
 497 0.001 , CA1 SLM and CB < 0.001 , cortex and striatum < 0.01 , cortex and CB < 0.001 ,
 498 striatum and CB < 0.001 , one-way ANOVA).

499 Our data thus far revealed that the dimensions of spines and their relative abundance
 500 differ according to the brain regions. Next, we calculated the average PSD area unit dendritic
 501 length and the average neck length unit dendritic length in each brain region (Table 3).
 502 These values are influenced by both the intrinsic structural properties of spines (PSD size or
 503 neck length) and the spine density. We observed that the average PSD area unit dendritic
 504 length is highest in the CB, followed by that in the CA1 PSR, striatum, cortex, and CA1 SLM
 505 (CA1 PSR: 0.18 ± 0.055 , CA1 SLM: 0.08 ± 0.031 , cortex: 0.11 ± 0.046 , striatum: $0.15 \pm$
 506 0.057 , CB: 0.77 ± 0.221). Similarly, the average neck length unit dendritic length is highest in
 507 the CB, followed by that in the striatum, CA1 PSR, cortex, and CA1 SLM (CA1 PSR: $1.35 \pm$
 508 0.442 , CA1 SLM: 0.37 ± 0.268 , cortex: 1.25 ± 1.205 , striatum: 2.16 ± 0.906 , CB: $5.29 \pm$
 509 1.539). Furthermore, the ratio of the summed PSD area to the summed neck length
 510 averaged from each dendrite was also similar between CA1 PSR and CB (Table 3).

511

512 **Organizational principle of dendritic spines along the dendrites in different** 513 **brain regions**

514 It is of great interest to reveal how the excitatory synaptic inputs are organized along
 515 a dendritic arbor. Dendrites actively integrate synaptic weights and serve as an independent
 516 computational unit (Stuart and Spruston, 2015). Dendrites are roughly cylindrical structures

517 whose diameter progressively decreases towards the distal tips (Hillman, 1979; Larkman et
 518 al., 1992). Small-diameter dendrites have high input resistance, and consequently, a small
 519 number of inputs are sufficient to evoke dendritic action potentials. In contrast, in the case of
 520 large-diameter dendrites, a large number of inputs are necessary to achieve the membrane
 521 depolarization high enough to reach the threshold for dendritic action potential initiation. We
 522 selected PSD area density (summation of multiple PSD areas along a dendrite divided by
 523 the dendritic length) as a measure of synaptic strength, instead of spine density. This
 524 selection of the PSD-based parameter is supported by the notion that the PSD area
 525 correlates with the functional synaptic strength (Nusser et al., 1998; Matsuzaki et al., 2001).
 526 Spine density measurement assigns equal synaptic weights to each spine irrespective of
 527 their sizes. However, both the PSD area and the spine size are highly variable and mutually
 528 correlated (Fig. 2-1A-E). As such, in comparison to the spine with the small PSD area, it is
 529 more reasonable to assign higher synaptic weights to the spine with the large PSD area.
 530 Thus, in comparison to the spine density, PSD area density is a better estimate of the
 531 synaptic strength of dendrites.

532 The spiny regions that we have studied differ in terms of microanatomy and cellular
 533 topography. We first limited our analysis of the relationship between dendritic diameter and
 534 PSD area per unit length of dendrite to CA1 PSR and CB. In both regions, somata of the
 535 principal neurons are confined to a specific layer. Therefore, dendrites sampled at the
 536 neuropil ~ 100 μm away from the edge of the cell layer can be anticipated to be relatively
 537 homogeneous in terms of their structure and function. However, contrary to our expectations,
 538 dendrites in CA1 PSR could be divided into two distinct populations based on the dendritic
 539 diameter (Fig. 2-3). Dendrites with a diameter of less than 1 μm were categorized as one
 540 group and those with a diameter larger than 1.4 μm as another group. Since this second
 541 population (dendritic diameter > 1.4 μm) is highly likely to be contaminated by the dendrites
 542 of the main apical trunk, which are known to have very few to no spines, we limited our
 543 analysis to the first group (i.e., dendritic diameter < 1 μm). This group of dendrites further

544 demonstrated heterogeneity in the dendritic diameter, which may serve as a putative
 545 indicator of the distance of the dendrites from the dendritic branch points. A positive
 546 correlation was observed between dendritic diameter and total PSD area per unit length of
 547 dendrite in both CA1 PSR and CB (CA1 PSR: $r = 0.78$, $p < 0.001$, Pearson's correlation; CB:
 548 $r = 0.76$, $p < 0.01$, Spearman's rank order test; Fig. 3A). Next, the layered organization of the
 549 cortex prompted us to examine if the statistically significant correlation between dendritic
 550 diameter and total PSD area per unit length of a dendrite, observed in CA1 PSR and CB,
 551 can also be found in the cortex. Although the cell bodies in the neocortex form discrete
 552 layers, the dendrites sampled in layer 1 could belong to cells in any of the underlying layers.
 553 Thus, due to the variation in the cell-type, the dendrites sampled from layer 1 are likely to be
 554 electrically heterogeneous in terms of their distance from the soma. However, despite this
 555 heterogeneity, we found that the PSD area per unit length of dendrite correlates with the
 556 dendritic diameter in the cortex ($r = 0.59$, $p < 0.01$, Pearson's correlation; Fig. 3A). In the
 557 case of the striatum, the cell body is not confined to a specific layer. Therefore, the
 558 relationship between the summed PSD areas and the relative position along dendrites is
 559 difficult to correlate. In other words, a given imaged region of the striatum is highly likely to
 560 contain dendrites that are located at varying distances from their parent soma. In the case of
 561 CA1 SLM, the presence of shaft excitatory synapses in their dendrites makes the calculation
 562 of total anatomical strength ambiguous. It has been previously shown that the inputs in
 563 dendritic shaft summate in a sublinear manner (Araya et al., 2006a), which is different
 564 compared to the linear integration of excitatory inputs on spines. Likely attributable to these
 565 reasons, no correlation between dendritic diameter and PSD area was observed in the
 566 striatum ($r = 0.06$, $p = 0.79$, Pearson's correlation; Fig. 3A) and CA1 SLM ($r = 0.26$, $p = 0.42$,
 567 Pearson's correlation; data not shown). Summation of PSD areas both from the spine head
 568 and dendritic shaft in CA1 SLM also did not result in any significant correlation with the
 569 dendritic diameter ($r = 0.44$, $p = 0.15$, Pearson's correlation). Nevertheless, our data
 570 demonstrate that the dendritic diameter serves as a useful indicator of the PSD content in
 571 CA1 PSR, cortex, and CB. Moreover, the result from striatum and CA1 SLM also argues that

the higher PSD content in large-diameter dendrites is not simply due to the availability of the larger surface area for synaptic contacts.

Spine neck is another important compartment of a dendritic spine that governs the magnitude of the synaptic strength. As observed for the total PSD area in a dendrite, the total neck length also scaled positively with a dendritic diameter in CA1 PSR (CA1 PSR, $r = 0.69$, $p < 0.01$, Pearson's correlation; Fig. 3B). In cortex and CB there was a trend for an increase in total neck length per unit dendritic length with the dendritic diameter, but the correlation was not statistically significant (cortex, $r = 0.31$, $p = 0.19$; CB, $r = 0.48$, $p = 0.13$; Spearman's rank order test; Fig. 3B).

Next, we examined if the statistically significant positive correlation in Fig. 3A, B is due to the higher spine density in large-diameter dendrites. The spine density positively correlates with the dendritic diameter in CA1 PSR ($r = 0.71$, $p < 0.01$, Pearson's correlation; Fig. 3-1A). However, although there was a trend towards higher spine density in the large-diameter dendrites in cortex and CB, the data did not reach statistical significance (cortex, $r = 0.43$, $p = 0.07$; CB, $r = 0.47$, $p = 0.14$; Spearman's rank order test; Fig. 3-1B, C). As noted earlier, the PSD area differs depending on the spine size, and as such, the contribution of each spine to the total synaptic strength is not equal. As a result, the plot of spine density versus dendritic diameter and the PSD area density versus dendritic diameter may not necessarily align with each other. It is reasonable to assume that both the spine density and the size of PSD contribute to the correlation between PSD area density and the dendritic diameter in multiple brain regions. The contribution of these two factors is clearly illustrated in the case of CA1 PSR, where both the spine density (Fig. 3-1A) and the average PSD area of spines ($r = 0.54$, $p = 0.03$, Pearson's correlation; Fig. 3C) show a significant positive correlation with dendritic diameter. Additionally, the average neck length is also positively correlated with the dendritic diameter in CA1 PSR ($r = 0.58$, $p = 0.02$, Pearson's correlation; Fig. 3D). Taken together, we propose that the intrinsic structural properties of spines differ across different dendrites, and both the spine density and the individual PSD size contribute

599 to the higher synaptic strength of a large-diameter dendritic segment in CA1 PSR, cortex
600 and CB.

601 The data thus far showed that the four parameters (the summed PSD area unit
602 dendritic length, average PSD area, summed neck length unit dendritic length, and average
603 neck length) increase with the dendritic diameter in CA1 PSR. As mentioned previously, the
604 ratio of the PSD area to the spine neck length may be a useful index for the estimation of the
605 synaptic strength of a spine. Since both the PSD area and the spine neck length show a
606 positive correlation to the dendritic diameter, the ratio between these two parameters can be
607 assumed to remain relatively similar across different dendrites. Experimentally, this
608 hypothesis was confirmed to be true in CA1 PSR (Fig. 3-2A). Besides, the neck diameter
609 (another important structural parameter that influences the synaptic strength of a dendritic
610 spine) also does not show an apparent correlation with the dendritic diameter (Fig. 3-2B).
611 These facts suggest that, despite the positive relationship of the spine head volume and the
612 neck length with the dendritic diameter, synaptic strength may not vary systematically among
613 dendrites of different diameters in the CA1 PSR.

614

615 **Analysis of information transfer in a model CA1 neuron**

616 Since the ratio of PSD area to neck length was relatively similar across dendrites of
617 different diameters, we were motivated to clarify the physiological relevance of synaptic
618 constancy across dendrites in CA1 PSR. To address this, we developed an abstract two-
619 layer model of a CA1 neuron (Fig. 3-3). In this model, excitatory synaptic inputs cause an
620 increase in membrane potentials in their parent dendritic branches and result in the firing of
621 dendritic spikes if the membrane potentials exceed a certain threshold (Häusser and Mel,
622 2003; Barnes et al., 2017). Such dendritic spikes were then converged and processed for
623 somatic spiking. In our model, we assumed two different scenarios of synaptic strength
624 distribution in dendrites (cases 1 & 2). In case 1, all synaptic strengths obey an identical

625 lognormal distribution (Fig. 3-3B, left). In case 2, synaptic strengths at any particular branch
 626 obey a lognormal distribution, but its shape parameter (μ_e , the median of the lognormal
 627 distribution) differs across branches (Fig. 3-3B, right). Synaptic strengths in case 1 have
 628 uniform median values, but those in case 2 do not. We then simulated the dendritic and
 629 somatic spikes of the two-layer model neuron in response to Poisson inputs to all the
 630 synapses. Next, we targeted the input sequence only to the strongest synapse of each
 631 branch, and the relationship between the synaptic input to the strongest synapse and the
 632 occurrence of the dendritic spike was studied by MI (Fig. 3-3C). MI showed a specific tuning
 633 curve as a function of synaptic input frequency (Fig. 3-3C, left). At low input frequency,
 634 dendritic branches could not elicit dendritic spikes. Hence no information was transmitted (MI
 635 = 0). It was observed that at moderate input frequency, a large number of weak synaptic
 636 inputs effectively supported the occurrence of dendritic spike initiated by the strongest
 637 synaptic input, thereby causing an increase in the MI transfer. However, the higher
 638 frequency inputs disturbed the neuronal information transmission from the dendrites towards
 639 the soma. Similar to our findings, Teramae et al. (2012) have also previously reported that a
 640 moderate level of noise enhances the information transfer of a nonlinear system driven by
 641 the weak and aperiodic input. Furthermore, the magnitude of synaptic strength in the
 642 dendrite also clearly influenced the synaptic input frequency-dependent tuning curve (Fig. 3-
 643 3C, right). Particularly, lowering the synaptic strength in a dendrite increased the input
 644 frequency value required for achieving an optimal MI (compare the input frequency values
 645 required for lower ($\mu_e = -6.4$) and higher ($\mu_e = -5.6$) synaptic strengths). This result shows
 646 that there exists an optimal frequency value for each distinct synaptic strength.
 647 Consequently, if synaptic strengths in all the branches obey a single lognormal distribution,
 648 the MI between the synaptic inputs and the somatic spikes is highly tuned to a single input
 649 frequency (Fig. 3-3D, left). In contrast, MI value decreases when the synaptic strength differs
 650 across branches (Fig. 3-3D, right). These results suggest that the constancy in synaptic
 651 strength across branches enables the effective transfer of information from the strongest
 652 synaptic input to the soma.

653

654

655 **Relative role of spine head and neck in excitatory postsynaptic potentials at**
 656 **the soma**

657 The observation that both the PSD area and neck length correlates positively with a
 658 dendritic diameter in CA1 PSR is particularly interesting. These two structural components of
 659 spines have an opposing influence on the voltage change at the dendrite. Whereas the
 660 larger PSD area leads to a higher current influx into the dendrite, the longer necks cause a
 661 significant attenuation of membrane potentials due to the electrical resistance of the neck
 662 (Araya et al., 2006b, 2014). If we simply overlook the influence of spine necks, the positive
 663 correlation between summed PSD area and dendritic diameter suggests higher synaptic
 664 strength in large dendrites. However, it is also equally possible that voltage attenuation
 665 caused by the spine neck supersedes the depolarizing influence of the spine head. In this
 666 scenario, as a result of the differences in the neck lengths, the spines located in the small-
 667 diameter dendrites are expected to exert a considerably stronger influence on the dendritic
 668 membrane potential changes than the spines located in the large-diameter dendrites.

669 To assess the relative role of the spine head and spine neck in EPSPs, we measured
 670 uEPSPs from individual spines (Fig. 4A) and examined the uEPSPs recorded at the soma
 671 against neck lengths and spine head widths (Fig. 4-1). As previously reported in the cortex
 672 (Araya et al., 2006b, 2014), the peak uEPSP amplitudes were negatively correlated with the
 673 spine neck lengths ($r = -0.33$, $p < 0.01$, Fig. 4-1A, B) but not with the head widths ($r = -0.07$,
 674 $p = 0.57$, Spearman's rank order test; Fig. 4-1C). To determine the role of spine neck in
 675 EPSPs at a single spine level, we divided spines that had similar head volumes ($p = 0.60$;
 676 Mann–Whitney U test; Fig. 4B) into two groups based upon spine length to head width ratio
 677 (Woods et al., 2011). The ratio of spine length to head width was significantly larger in long
 678 neck spine groups compared with the short neck spines group (ratio in long neck spine

groups = 1.61 ± 0.586 , short neck spine groups = 0.94 ± 0.208 , $p < 0.001$, Mann–Whitney U test; Fig. 4B). We found that the uEPSPs were significantly smaller in the long neck spines than in the short neck spines (long neck spines group = 0.92 ± 0.54 mV, short neck spines group = 1.66 ± 0.94 mV, $p < 0.001$, Mann–Whitney U test; Fig. 4B). These data strongly suggest that neck length has a more significant influence than spine head size on voltage changes at the soma.

Morphological features of axon-coupled spines

We next analyzed if the frequency of axon-coupled spines (spines that reside in the same dendritic segment and receive synaptic inputs from the same axon) correlates with the dendritic diameter. Axon-coupled spines are of special interest as they experience the same presynaptic inputs and postsynaptic membrane depolarizations, leading to a highly synchronized activation of signaling pathways related to spine structural changes. An increasing number of studies have shown that spatially close inputs onto spines summate non-linearly and increase the dendritic membrane potential beyond the threshold required for the generation of local dendritic spikes (Gasparini et al., 2004; Govindrajan et al., 2006; Larkum and Nevian, 2008). Thus, a higher frequency of axon-coupled spines can also result in higher synaptic strength in a particular dendritic segment. We followed the presynaptic terminals of each spine along the entire length of the dendritic tree contained within the imaging volume (Fig. 5A-D). Subsequently, we counted the frequency that the identified axons contact multiple spines located in the same dendrite. The frequency of axon-coupled spines was 4.7% in CA1 PSR, 25.7% in CA1 SLM, 5.4% in the cortex, 8.9% in the striatum, and 26.1% in CB. Interestingly, the canonical view that there exists a one-to-one connection between a parallel fiber to Purkinje cell is violated in more than 25% of the spines (Table 4). To examine if the dendritic diameter can predict the relative frequency of axon-coupled spines, we plotted the frequency of axon-coupled spines against dendritic diameter. The plot

revealed no significant correlation between these two parameters in CA1 PSR, CA1 SLM, striatum and CB (CA1 PSR: $r = 0.46$, $p = 0.07$; CA1 SLM: $r = 0.28$, $p = 0.38$; striatum: $r = -0.07$, $p = 0.78$; CB: $r = 0.06$, $p = 0.85$; Spearman's rank order test). This analysis was not applied to the cortex, as only 4 dendrites (out of 12) contained axon-coupled spines. Our data demonstrate that the dendritic diameter cannot predict the frequency of the axon-coupled spines. Studies in CA1 PSR (Bartol et al., 2015), CA1 SLM (Bloss et al., 2018), and cortex (Kasthuri et al., 2015) have reported that the axon-coupled spines are of similar head volume. We further extended this finding and show that the axon-coupled spines have similar PSD areas in CA1 PSR (Fig. 5E) and CB (Fig. 5F). The variance of PSD size was smaller in axon-coupled spines compared to the rest of the spines both in CA1 PSR (variance in axon-coupled spines = 0.0008, rest of the spines = 0.0011) and CB (variance in axon-coupled spines = 0.00209, rest of the spines = 0.00257).

Intracellular organelles in dendrites and spines

Lastly, we looked into the distribution of ER in the spines. In all the brain regions that we have studied, we found that ER is a continuous structure along the dendrites and extends into the spines (Fig. 6A-E). The frequency of spines positive for ER varies depending on the brain region (Table 5). ER-containing spines had significantly larger head volume and wider neck diameter in CA1 PSR, CA1 SLM, cortex, and striatum (Table 5). However, the neck length did not differ significantly between those spines that contained ER and those that did not.

To further corroborate the finding from FIB/SEM images on the frequency of ER-containing spines in the cortex, striatum, and CB, we performed pre-embedding immunogold labeling with an antibody against IP₃R1 (Fig. 6F-J). We observed that all the spines showed immunoreactivity for IP₃R1 in CB. However, in the case of cortex and striatum, we found that the percentages of IP₃R1 positive spines were somewhat lower than the percentages of

731 spines estimated to contain ER based on FIB/SEM images (frequency of IP₃R1 positive
732 spines in cortex = 30.2%, striatum = 35.2%; frequency of ER-containing spines in cortex =
733 40.3%, striatum = 55.1%). This is not unexpected because IP₃R1 content is much lower in
734 the dendrites and spines of cortex and striatum than in the dendrites and spines of CB (Fig.
735 6F-J). As the labeling efficiency of the pre-embedding immunogold labeling method is
736 unlikely to be 100% due to the low number of IP₃R1 in individual spines, the frequency of
737 spines containing IP₃R1 is likely to be somewhat under-represented in the case of cortex
738 and striatum.

739 Interestingly, a significant fraction of ER containing spines is often located in the
740 vicinity (53.3% of spines in CA1 PSR, 33.3% of the spines in CA1 SLM, 69.7% of spines in
741 the cortex, 81.5% of spines in the striatum (Fig. 6K, L)), suggesting that the ER-containing
742 spines form a hotspot along the dendritic segment.

743

744 Discussion

745 Morphology serves as the basis for physiological functioning. Here, using FIB/SEM to
746 perform volume imaging from several brain regions, we provide a thorough overview of
747 dendritic spine morphology. The use of FIB/SEM overcomes inherent problems associated
748 with serial section transmission electron microscopy (ssTEM) such as variations in section
749 thickness and image distortion during sectioning and image acquisition. Manual
750 segmentation of structures provides a more accurate reflection of the spine dimension
751 compared to the automated machine-learning based segmentation. Cross comparison of
752 different brain regions was performed from the same brain, thus ascertaining uniformity in
753 terms of age, sample preparation, and methods of analysis. Our reconstruction data of a
754 large number of dendrites and their dendritic spines show that the dendritic spines, despite
755 their great structural diversity, are organized along a dendrite in a regulated manner. The

756 breadth of data provided by our study can serve as a reference for the functional
757 interpretation of various experimental data acquired by synaptic physiologists.

758

759 **Regional uniqueness in spine morphology**

760 Even after an extensive analysis of hundreds of spines, to accurately identify the
761 brain region where a given spine was sampled might still be a daunting task. High variability
762 and significant overlap in spine dimensions across brain regions preclude identification of a
763 structural fingerprint unique to each area. However, with a certain degree of confidence,
764 spines with large head volume and short neck length can be associated with CA1 SLM; large
765 head volume and medium neck length with CB; medium head volume and long neck length
766 with cortex; medium head volume, long and swollen wide necks in the midway with striatum;
767 and small head volume and short neck length with CA1 PSR. Moreover, incorporation of
768 other structural parameters in the dendrites, such as spine density, frequency of branching,
769 spine perforation, etc. can aid in identifying the brain region where a spine is sampled.

770 Short spine necks facilitate rapid transfer of electrical (Araya et al., 2006b, 2014; Fig.
771 4 in this study) and chemical (Svoboda et al., 1996) signals from the spine head towards the
772 dendritic shaft. Spine necks in CA1 PSR and CB are relatively shorter than the other brain
773 regions that we have studied. Besides, the dendrites in these two areas possess high spine
774 density (Fig. 2F, Table 2). Short spine necks and small inter-spine distance create a
775 favorable situation for signal cross-talk among spines. Indeed, by two-photon glutamate
776 uncaging and time-lapse imaging, heterosynaptic interaction between CA1 PSR spines has
777 been directly demonstrated (Oh et al., 2015). It would be interesting to examine if
778 heterosynaptic interactions could be induced more efficiently and reliably in CA1 PSR and
779 CB than in CA1 SLM, cortex, and striatum.

780 Unlike in the CB and CA1, the spine heads of the cortex and striatum receive multiple
781 presynaptic inputs with distinct neurotransmitter contents from various brain nuclei. The long
782 necks in the cortex and striatum hinder the diffusion of signals from the spine heads towards

the dendritic shafts and retain the signal within a spine head for a considerable amount of time. As a result, this increases the time-window for intra-spine interaction of afferent signals that use different neurotransmitters and are originated from multiple brain areas. The wider time-window of signal interaction is particularly useful in the striatum, where the communication of dopaminergic and glutamatergic inputs is necessary to drive reward learning (Yagishita et al., 2014).

Common synaptic organizational principle

We revealed that the PSD area per unit length of dendrite increases as a function of dendritic diameter. One may argue that this is not unexpected as bigger dendrites, compared to the smaller ones, contain larger membrane surface area and resources necessary to generate more PSD structures. However, the fact that this trend is not observed in the striatum and CA1 SLM suggests that the availability of higher membrane surface area in dendrites alone cannot account for the gradient in PSD density. We believe that this type of organizational principle is unique for dendrites in CA1, CB, and cortex, whose somata are organized in discrete layers.

What function does it serve to have intra-dendritic scaling of PSD density? One obvious possibility is that the intra-dendritic scaling plays a role to normalize membrane depolarization by creating a counterbalance between the magnitude of synaptic inputs and the input impedance of the dendritic shaft. Thin dendrites require relatively few inputs to generate enough depolarization. In the case of thick dendrites, a large number of stronger inputs are necessary to create dendritic spikes. Therefore, it is physiologically relevant to have a high number of big synapses in the large diameter dendrites. Perhaps intracellular organelles that are abundant in thick diameter dendrites facilitate an increase in the PSD area. A large fraction of spines contains ER in multiple brain regions, and ER-containing spines have larger spine heads (Table 5). On the other hand, spine neck length is not positively regulated by spine ER, suggesting independent regulatory pathways of spine head

810 enlargement and spine neck growth, both of which contribute to the local regulation of
811 synaptic strength.

812 We also identified a positive correlation between the spine neck length and the
813 dendrite diameter. This observation rather supports the idea that higher PSD density and
814 longer spine neck length compensate with each other in thick dendrites and result in a less
815 noticeable difference in total synaptic strength between the thin and thick dendrites. Synaptic
816 constancy across dendrites suggests that even though the synaptic strength of individual
817 spines or synaptic connections dynamically changes as a result of synaptic plasticity, the
818 total synaptic strength in the dendrite remains constant. This synaptic constancy hints at the
819 existence of a homeostatic mechanism at the level of individual dendritic branches that
820 compensate for changes in the synaptic weights of individual spines. Using ssTEM images,
821 Bourne and Harris (2011) revealed that upon long-term potentiation, the stimulated spines
822 grew in volume at the expense of unstimulated spines such that the PSD area per unit
823 dendritic length remained conserved between control and stimulated conditions. What could
824 be the functional relevance of maintaining synaptic constancy among dendritic branches?
825 Our computational study indicates that synaptic constancy among CA1 dendrites enables
826 them to integrate a moderate level of synaptic noise to the authentic synaptic signal and
827 enhance the overall signal transmission from the strongest synapse towards the soma.
828 Constancy in synaptic strength may also be beneficial for the coordinated firing of CA1 place
829 cells during theta oscillations (Buzsáki, 2002) as these cells utilize phase-dependent firing
830 activity relative to background oscillatory inputs for information processing.

831 Our electrophysiology data showed that the uncaging EPSP amplitudes at the soma
832 are independent of the spine head widths but are rather inversely correlated with the spine
833 neck lengths. As a result, it can be expected that EPSPs produced by spines located in the
834 large diameter dendrites would be attenuated more severely because of their longer necks.
835 The differential filtering of synaptic potentials may serve a purpose to normalize the EPSP
836 amplitude at the soma irrespective of the site of its origin in the dendrite.

837 The integrative property of dendrites is heavily influenced by their distance from the
 838 cell body. Thus, the precise distance of each spine and dendrite is highly informative in
 839 understanding their relative contribution in somatic depolarization. In this study, we did not
 840 attempt to measure the precise distance of each dendrite and spine from their respective cell
 841 bodies, which require time-consuming correlative light and electron microscopy (CLEM) and
 842 retrospective EM reconstruction. In general, dendritic diameter serves as a reliable indicator
 843 of the relative distance of the individual dendrites from their parent soma (Grillo et al., 2018).
 844 However, in our data from CA1 PSR, the dendritic diameter may not necessarily reflect the
 845 distances of the dendrites from their soma. Since the imaging volume in CA1 PSR was
 846 located at a distance of $\sim 100 \mu\text{m}$ from the edge of the CA1 pyramidal cell layer, the straight-
 847 line distances of dendrites do not vary considerably from their corresponding cell bodies.
 848 Thus, rather than the distance from the soma, the dendritic diameter may indicate the
 849 relative distance from the dendritic branch points on the primary apical dendrite. As shown
 850 previously (Menon et al., 2013; Benavides-Piccione et al., 2020), we surmise that the thick
 851 dendrites in our data sets represent dendritic segments near the branch points, and thin
 852 dendrites represent dendritic segments away from the branch points.

853 The spine distribution pattern in hippocampal CA1 dendrites is likely conserved
 854 across species and different developmental stages. Somewhat similar to our findings, Katz
 855 et al. (2009) have previously shown that in the apical oblique dendritic branches of 6-month-
 856 old rats, both the spine density and the average synapse size decrease towards the distal
 857 ends. Interestingly, in the basal dendrites in the CA1 stratum oriens of 6-month-old rats, the
 858 spine volume was significantly smaller, and the spine density was significantly lower in the
 859 small-diameter dendrites than that in the large-diameter dendrites (Menon et al., 2013). In
 860 another study in P21 mice (Walker et al., 2017), it was shown that the active zone area of
 861 the presynaptic bouton, the volume, and the PSD area of dendritic spines scales positively
 862 with the dendritic diameter. Similarly, it was shown that both in the P22 and P100 mice, the
 863 size of the presynaptic active zone increases with the dendritic diameter and decreases with
 864 the distance from the cell body (Grillo et al., 2018). These studies, taken together, suggest

865 that the organizational principle of dendritic spines in the CA1 pyramidal cells is similar both
866 in the apical oblique and the basal dendrites and is maintained throughout developmental
867 stages both in the mice and rats.

868 Previous studies in CA1 PSR (Bartol et al., 2015), CA1 SLM (Bloss et al., 2018), and
869 cortex (Kasthuri et al., 2015) have shown that the axon-coupled spines have similar head
870 volumes and neck lengths. We show that this observation holds in the CB as well,
871 suggesting that this may be one of the conserved principles underlying axon-spine
872 connectivity. The fact that axon-coupled spines have similar PSD areas hints that these
873 spines have the same history of plasticity. We also revealed that ER-containing spines are
874 located in the vicinity to form a hotspot. Moreover, in comparison to ER-lacking spines, ER-
875 containing spines have larger heads and wider necks. Neuronal activity or plasticity-related
876 stimulus may serve as the address marker for dictating which specific spine should harbor
877 ER. Indeed, Imaging experiments *in vitro* and *in vivo* have shown that experience results in
878 the activation of nearby spines located in the same branchlet (Takahashi et al., 2012; Lee et
879 al., 2016; Frank et al., 2018) and the potentiated spines have larger heads and wider necks
880 than the un-potentiated spines (Fifková and Anderson, 1981). Perhaps, ER is selectively
881 recruited to such potentiated spines to sustain an increased demand for calcium ions
882 following synaptic potentiation.

883 In conclusion, our study provides an accurate morphological description and
884 physiological role of various parameters that shape synaptic transmission and the principle
885 underlying the placement of dendritic spines in a dendritic branch. Ultimately, with the
886 development of a high throughput image acquisition and image analysis method, it is
887 necessary to extrapolate these findings to all the spiny neurons in the brain. Although a great
888 deal of labor is expended for a study of this nature, the wealth of information that it provides
889 is rewarding.

890

891 **References**

- 892 Araya R, Eiselthal KB, Yuste R (2006a) Dendritic spines linearize the summation of
 893 excitatory potentials. *Proc Natl Acad Sci USA* 103:18799–18804.
- 894 Araya R, Jiang J, Eiselthal KB, Yuste R (2006b) The spine neck filters membrane potentials.
 895 *Proc Natl Acad Sci U S A* 103:17961–17966.
- 896 Araya R, Vogels TP, Yuste R (2014) Activity-dependent dendritic spine neck changes are
 897 correlated with synaptic strength. *Proc Natl Acad Sci USA* 111:E2895–E2904.
- 898 Barnes SJ, Franzoni E, Jacobsen RI, Erdelyi F, Szabo G, Clopath C, Keller GB, Keck T
 899 (2017) Deprivation-induced homeostatic spine scaling *in vivo* is localized to dendritic
 900 branches that have undergone recent spine loss. *Neuron* 96:871–882.
- 901 Bartol TM, Bromer C, Kinney J, Chirillo MA, Bourne JN, Harris KM, Sejnowski TJ (2015)
 902 Nanoconnectomic upper bound on the variability of synaptic plasticity. *Elife* 4, e10778.
- 903 Benavides-Piccione R, Regalado-Reyes M, Fernaud-Espinosa I, Kastanauskaite A, Tapia-
 904 Gonzalez S, Leon-Espinosa G, Rojo C, Insausti R, Segev I, DeFelipe J (2020) Differential
 905 structure of hippocampal CA1 pyramidal neurons in the human and mouse. *Cereb Cortex*
 906 30:730–752.
- 907 Bloss EB, Cembrowski MS, Karsh B, Colonell J, Fetter RD, Spruston N (2018) Single
 908 excitatory axons form clustered synapses onto CA1 pyramidal cell dendrites. *Nat Neurosci*
 909 21: 353–363.
- 910 Bock DD, Lee WCA, Kerlin AM, Andermann ML, Hood G, Wetzel AW, Yurgenson S, Soucy
 911 ER, Kim HS, Reid RC (2011) Network anatomy and *in vivo* physiology of visual cortical
 912 neurons. *Nature* 471:177–182.

- 913 Bourne JN, Harris KM (2011) Coordination of size and number of excitatory and inhibitory
 914 synapses results in a balanced structural plasticity along mature hippocampal CA1 dendrites
 915 during LTP. *Hippocampus* 21:354–373.
- 916 Buzsáki G (2002) Theta oscillations in the hippocampus. *Neuron* 33:325–340.
- 917 Fiala JC (2005) Reconstruct: a free editor for serial section microscopy. *J Microsc* 218:52–61.
- 918 Fifková E, Anderson CL (1981) Stimulation-induced changes in dimensions of stalks of
 919 dendritic spines in the dentate molecular layer. *Exp Neurol* 74:621–627.
- 920 Frank AC, Huang S, Zhou M, Gdalyahu A, Kastellakis G, Silva TK, Lu E, Wen X, Poirazi P,
 921 Trachtenberg JT, Silva AJ (2018) Hotspots of dendritic spine turnover facilitate clustered
 922 spine addition and learning and memory. *Nat Commun* 9:422.
- 923 Gasparini S, Migliore M, Magee JC (2004) On the initiation and propagation of dendritic
 924 spikes in CA1 pyramidal neurons. *J Neurosci* 24:11046–11056.
- 925 Govindarajan A, Kelleher RJ, Tonegawa S (2006) A clustered plasticity model of long-term
 926 memory engrams. *Nat Rev Neurosci* 7:575–583.
- 927 Grillo FW, Neves G, Walker A, Vizcay-Barrena G, Fleck RA, Branco T, Burrone J (2018) A
 928 distance-dependent distribution of presynaptic boutons tunes frequency-dependent dendritic
 929 integration. *Neuron* 99:275–282.
- 930 Harris KM, Stevens JK (1988) Dendritic spines of rat cerebellar Purkinje cells: serial electron
 931 microscopy with reference to their biophysical characteristics. *J Neurosci* 8:4455–4469.
- 932 Harris KM, Stevens JK (1989) Dendritic spines of CA1 pyramidal cells in the rat
 933 hippocampus: serial electron microscopy with reference to their biophysical characteristics. *J*
 934 *Neurosci* 9:2982–2997.

- 935 Harris KM, Jensen FE, Tsao B (1992) Three-dimensional structure of dendritic spines and
936 synapses in rat hippocampus (CA1) at postnatal day 15 and adult ages: implications for the
937 maturation of synaptic physiology and long-term potentiation. *J Neurosci* 12:2685–2705.
- 938 Harris K, Spacek J (2016) Dendrite structure. In: *Dendrites* (Stuart G, Spruston N, Häusser
939 M, eds.), pp. 1–46, Oxford: Oxford University Press.
- 940 Häusser M, Mel B (2003) Dendrites: bug or feature? *Curr Opin Neurobiol* 13:372–383.
- 941 Hillman DE (1979) Neuronal shape parameters and substructures as a basis of neuronal
942 form. In: *The Neurosciences: Fourth Study Program* (Schmitt FO, Worden FG, eds.), pp
943 477–498, Cambridge: MIT Press.
- 944 Jones EG, Powell TP (1969) Morphological variations in the dendritic spines of the
945 neocortex. *J Cell Sci* 5: 509–529.
- 946 Kasthuri N, et al. (2015) Saturated reconstruction of a volume of neocortex. *Cell* 162:648–
947 661.
- 948 Katz Y, Menon V, Nicholson DA, Geinisman Y, Kath WL, Spruston N (2009) Synapse
949 distribution suggests a two-stage model of dendritic integration in CA1 pyramidal neurons.
950 *Neuron* 63:171–177.
- 951 Konur S, Rabinowitz D, Fenstermaker VL, Yuste R (2003) Systematic regulation of spine
952 sizes and densities in pyramidal neurons. *J Neurobiol* 56: 95–112.
- 953 Larkman AU, Major G, Stratford KJ, Jack JJB (1992) Dendritic morphology of pyramidal
954 neurones of the visual cortex of the rat: IV. Electrical geometry. *J Comp Neurol* 323: 137–
955 152.
- 956 Larkum ME, Nevian T (2008) Synaptic clustering by dendritic signalling mechanisms. *Curr*
957 *Opin Neurobiol* 18:321–331.

- 958 Lee KFH, Soares C, Thivierge JP, Béique JC (2016) Correlated synaptic inputs drive
 959 dendritic calcium amplification and cooperative plasticity during clustered synapse
 960 development. *Neuron* 89:784–799.
- 961 Magee JC, Cook EP (2000) Somatic EPSP amplitude is independent of synapse location in
 962 hippocampal pyramidal neurons. *Nat Neurosci* 3:895–903.
- 963 Markram H, et al. (2015) Reconstruction and simulation of neocortical microcircuitry. *Cell*
 964 163:456–492.
- 965 Matsuzaki M, Ellis-Davies GCR, Nemoto T, Miyashita Y, Iino M, Kasai H (2001) Dendritic
 966 spine geometry is critical for AMPA receptor expression in hippocampal CA1 pyramidal
 967 neurons. *Nat Neurosci* 4:1086–1092.
- 968 Matsuzaki M, Honkura N, Ellis-Davies GCR, Kasai H (2004) Structural basis of long-term
 969 potentiation in single dendritic spines. *Nature* 429:761–766.
- 970 Menon V, Musial TF, Liu A, Katz Y, Kath WL, Spruston N, Nicholson DA (2013) Balanced
 971 synaptic impact via distance-dependent synapse distribution and complementary expression
 972 of AMPARs and NMDARs in hippocampal dendrites. *Neuron* 80:1451–1463.
- 973 Nusser Z, Lujan R, Laube G, Roberts JDB, Molnar E, Somogyi P (1998) Cell type and
 974 pathway dependence of synaptic AMPA receptor number and variability in the hippocampus.
 975 *Neuron* 21:545–559.
- 976 Oh WC, Parajuli LK, Zito K (2015) Heterosynaptic structural plasticity on local dendritic
 977 segments of hippocampal CA1 neurons. *Cell Rep* 10:162–169.
- 978 Oh WC, Lutz S, Castillo PE, Kwon HB (2016) De novo synaptogenesis induced by GABA in
 979 the developing mouse cortex. *Science* 353:1037–1040.
- 980 Okabe S (2020) Recent advances in computational methods for measurement of dendritic
 981 spines imaged by light microscopy. *Microscopy* 69:196–213.

- 982 Parajuli LK, Tanaka S, Okabe S (2017) Insights into age-old questions of new dendritic
 983 spines: From form to function. *Brain Res Bull* 129:3–11.
- 984 Parajuli LK, Wako K, Maruo S, Kakuta S, Koike M (2020a) Unique synaptic topography of
 985 crest-type synapses in the interpeduncular nucleus. *Biochem Biophys Res Commun*
 986 530:130–135.
- 987 Parajuli LK, Wako K, Maruo S, Kakuta S, Taguchi T, Ikuno M, Yamakado H, Takahashi R,
 988 Koike M (2020b) Developmental changes in dendritic spine morphology in the striatum and
 989 their alteration in an A53T α -synuclein transgenic mouse model of Parkinson's disease.
 990 *eNeuro* 7(4):1–14.
- 991 Rall W (1962) Theory of physiological properties of dendrites. *Ann NY Acad Sci* 96:1071–
 992 1092.
- 993 Routh BN, Johnston D, Harris K, Chitwood RA (2009) Anatomical and electrophysiological
 994 comparison of CA1 pyramidal neurons of the rat and mouse. *J Neurophysiol* 102:2288–2302.
- 995 Royer S, Paré D (2003). Conservation of total synaptic weight through balanced synaptic
 996 depression and potentiation. *Nature* 422:518–522.
- 997 Schikorski T, Stevens CF (1997) Quantitative ultrastructural analysis of hippocampal
 998 excitatory synapses. *J Neurosci* 17: 5858–5867.
- 999 Schindelin J, Arganda-Carreras I, Frise E, Kaynig V, Longair M, Pietzsch T, Preibisch S,
 1000 Rueden C, Saalfeld S, Schmid B, Tinevez JY, White DJ, Hartenstein V, Eliceiri K, Tomancak
 1001 P, Cardona A (2012) Fiji: an open-source platform for biological-image analysis. *Nat*
 1002 *Methods* 9:676–682.
- 1003 Stuart GJ, Spruston N (2015) Dendritic integration: 60 years of progress. *Nat Neurosci*
 1004 18:1713–1721.
- 1005 Svoboda K, Tank DW, Denk W (1996) Direct measurement of coupling between dendritic
 1006 spines and shafts. *Science* 272:716–719.

1007 Takahashi N, Kitamura K, Matsuo N, Mayford M, Kano M, Matsuki N, Ikegaya Y (2012)
1008 Locally synchronized synaptic inputs. *Science* 335:353–356.

1009 Takahashi-Nakazato A, Parajuli LK, Iwasaki H, Tanaka S, Okabe S (2019) Ultrastructural
1010 observation of glutamatergic synapses by focused ion beam scanning electron microscopy
1011 (FIB/SEM). *Methods Mol Biol* 1941:17–27.

1012 Teramae JN, Tsubo Y, Fukai T (2012) Optimal spike-based communication in excitable
1013 networks with strong-sparse and weak-dense links. *Sci Rep* 2:485.

1014 Walker AS, Neves G, Grillo F, Jackson RE, Rigby M, O'Donnell C, Lowe AS, Vizcay-Barrena
1015 G, Fleck RA, Burrone J (2017) Distance-dependent gradient in NMDAR-driven spine calcium
1016 signals along tapering dendrites. *Proc Natl Acad Sci USA* 114:E1986–E1995.

1017 Wilson CJ, Groves PM, Kitai ST, Linder JC (1983) Three-dimensional structure of dendritic
1018 spines in the rat neostriatum. *J Neurosci* 3:383–398.

1019 Woods GF, Oh WC, Boudewyn LC, Mikula SK, Zito K (2011) Loss of PSD-95 enrichment is
1020 not a prerequisite for spine retraction. *J Neurosci* 31:12129–12138.

1021 Yagishita S, Hayashi-Takagi A, Ellis-Davies GCR, Urakubo H, Ishii S, Kasai H (2014) A
1022 critical time window for dopamine actions on the structural plasticity of dendritic spines.
1023 *Science* 345:1616–1620.

1024

1025

1026

1027

1028

1029

1030

1031

1032

Figure Legends (Main Figures)

1033 **Figure 1: Structural diversity of dendritic spines in the brain**

1034 Membrane contours of presynaptic boutons (b), dendrites (d) and spines (s) can be clearly
1035 visualized in FIB/SEM images from the cortex (**A**) and CB (**B**). PSDs (indicated by black
1036 arrows and delimited by two vertical red bars) and ER (blue arrowheads) are also visible.
1037 Three-dimensional (3D) reconstructions of dendrite (orange), spines (violet) and PSDs (red)
1038 in the CA1 PSR (an oblique dendrite, **C**), CA1 PSR (a large-caliber dendrite, **D**), CA1 SLM
1039 (**E**), cortex (**F**), striatum (**G**) and CB (**H**) show that spines of various morphologies protrude
1040 from the same dendrite. Panels (**I**) to (**R**) show spines of various morphologies. Panel **J**
1041 shows an example of a perforated PSD. Spine heads, spine necks, and PSDs are denoted
1042 by violet, blue and red color, respectively. The bar graph in (**S**) shows the proportion of
1043 surface area occupied by spine head, PSD, spine neck, and dendritic shaft. Dendritic spines
1044 occupy approximately 50% of surface area in the CA1 PSR and striatum, 40% in CA1 SLM,
1045 45% in the cortex, and 80% in CB. Scale bars: 500 nm in A and B; Scale cubes: 0.5 μm on
1046 each side for all reconstructions except for the CA3 thorny excrescence spine (1 μm on each
1047 side).

1048

1049 **Figure 2: Morphometric analysis of dendritic spines in multiple**

1050 **brain regions**

1051 Box and whiskers plots show that the spine head volume (**A**), spine neck length (**B**), and
1052 spine neck diameter (**C**) are highly variable, and there exists a significant overlap in their
1053 dimensions across different brain regions. Note that, compared to other brain regions, the

1054 dendritic spines in CB display much less variability in spine head volume. **D**, The bar graph
1055 shows that the ratio of PSD area to neck length is not significantly different between spines
1056 in the CA1 PSR and CB. Error bars indicate standard error of mean (SEM). **E**, Three-
1057 dimensional plot shows that the dendrites from CA1 PSR, CA1 SLM, cortex, striatum, and
1058 CB are not easily distinguishable from each other based on the analysis of the average neck
1059 diameter, average PSD area, and average neck length of their spines. **F**, Box and whiskers
1060 plot shows that the spine density is high in the CB, moderate in the CA1 PSR and striatum,
1061 and low in the CA1 SLM and cortex. Mean values are indicated by + mark in **A**, **B**, **C**, and **F**.
1062 The box shows 25th, 50th, and 75th percentiles of the data set. In each graph, a significant
1063 difference exists in the spine dimensions between any pair of brain regions not designated
1064 as n.s. (not significant). **Figure 2-1** shows that the spine head volume correlates strongly
1065 with the PSD area, but only weakly with the neck length. A linear positive correlation
1066 between the amplitude of uEPSC and the spine head volume is shown in **Figure 2-2**. A
1067 scatter plot in **Figure 2-3** shows that the dendrites in the CA1 PSR can be grouped in two
1068 distinct populations based on their dendritic diameter.

1069

1070 **Figure 3: Spines are organized in a regulated manner in the** 1071 **dendrites**

1072 **A**, PSD area unit dendritic length shows a significant positive correlation with the dendritic
1073 diameter in the CA1 PSR, cortex, and CB (see also **Figure 3-1**). However, in the striatum,
1074 the PSD area unit dendritic length does not correlate with dendritic diameter. **B**, Neck length
1075 unit dendritic length is positively correlated with the dendritic diameter in the CA1 PSR. The
1076 data from CA1 PSR, cortex and striatum are plotted in reference to the left vertical axis, and
1077 the data from CB are plotted in reference to the right vertical axis in panels **A** and **B**.
1078 Average PSD area (**C**), and average neck length (**D**) show a positive correlation with the
1079 dendritic diameter in the CA1 PSR. Scatter plots in **Figure 3-2** show that the ratio of the total

1080 PSD area to total neck length (**A**), and the average neck diameter (**B**) do not correlate with
 1081 the dendritic diameter in the CA1 PSR. **Figure 3-3** shows that the synaptic constancy
 1082 enables effective information transfer from the dendrite to the soma.

1084 **Figure 4: Spine neck strongly filters membrane potential on CA1**

1085 **pyramidal neurons**

1086 **A**, Two-photon image of a dendritic segment showing the spines (blue crosses: spines of
 1087 similar head size, but different neck length; red crosses: spines of different head size, but
 1088 similar neck length) receiving glutamate uncaging stimulus. uEPSPs were evoked by
 1089 glutamate uncaging test pulses (5-10 trials at 0.1 Hz). Blue and red traces are representative
 1090 uEPSPs from blue and red targets, respectively. **B**, Quantitative analyses of the estimated
 1091 spine volume, spine length to width ratio, and uEPSPs of long (filled bars) and short (open
 1092 bars) neck spines (n = 35 spines in each group, 6 cells). Error bars indicate standard error of
 1093 mean (SEM). n.s., not significant. See **Figure 4-1** for the relationship of the uEPSP
 1094 amplitude with the spine neck length and the head width.

1096 **Figure 5: Intra-pair synapse sizes are similar in axon-coupled spine**

1097 **pairs**

1098 **A**, Three-dimensional (3D) reconstruction of a cortical axon (medium slate blue) that makes
 1099 synaptic contacts with spines from multiple dendrites. **B**, An example of an axon in the CA1
 1100 PSR that makes synaptic contacts with two spines (shown by white arrows) from the same
 1101 dendrite. **C**, An example of a parallel fiber in CB making synaptic contacts with three
 1102 different spines from the same dendrite. **D**, An example of a climbing fiber in CB making
 1103 synaptic contacts with seven different spines (turquoise protrusions from the dendrite) from

1104 the same dendrite. PSD areas of axon-coupled spine pairs are positively correlated in the
1105 CA1 PSR (E) and CB (F). Scale cubes: 0.5 μm for each side.

1106

1107 **Figure 6: Distribution of endoplasmic reticulum in dendrites and**
1108 **spines**

1109 Three-dimensional (3D) reconstruction showing ER (green) and mitochondria (turquoise) in
1110 an oblique dendrite in the CA1 PSR (A), cortical dendrite (B), striatal dendrite (C), large-
1111 caliber dendrite in the CA1 PSR (D) and Purkinje cell dendrite in the CB (E). ER (green) is a
1112 continuous structure along the dendrite (orange) and extends into spines in all the brain
1113 regions. Dendrites, spines, PSDs (red), ER (green), and mitochondria (turquoise) are shown
1114 on the left-hand side, and only ER (green) and mitochondria (red) for the same dendrite are
1115 shown on the right-hand side in each panel in A-E. TEM images showing immunoreactivity
1116 for IP₃R1 in the dendrites (d) and spines (s) of the cortex (F), striatum (G), and CB (H-J).
1117 The schematic diagram in (K) shows that the ER (blue line) is continuous along the dendrite
1118 and extends into spines. Panel (L) shows that in more than 50% of the cases, ER-containing
1119 spines are located next to one another in the CA1 PSR, cortex, and striatum. Scale cubes in
1120 A-E: 0.5 μm for each side, Scale bars in F-J: 500 nm.

1121

1122

1123

1124

1125

1126

1127

1128

Figure Legends (Extended Figures)

1129

Figure 2-1: Spine head volume correlates strongly with the

1130

postsynaptic density area but only weakly with the neck length

1131

Scatter plots show a significant positive correlation between head volume and PSD area in

1132

the CA1 PSR (**A**), CA1 SLM (**B**), cortex (**C**), striatum (**D**), and CB (**E**). Scatter plots show that

1133

there is no significant correlation between head volume and neck length in the CA1 PSR (**F**),

1134

CA1 SLM (**G**), and cortex (**H**). A significant negative correlation is observed between head

1135

volume and neck length in the striatum (**I**) and CB (**J**). Head volume in **F-J** is expressed on a

1136

logarithmic scale.

1137

1138

Figure 2-2: The amplitude of uncaging-evoked excitatory

1139

postsynaptic current positively correlates with the spine head

1140

volume

1141

A, Two-photon image of a CA1 pyramidal neuron from an acute hippocampal slice recorded

1142

in whole-cell voltage-clamp mode. uEPSCs (blue trace) from target spines were evoked by

1143

the application of glutamate uncaging test pulses (7-10 trials at 0.1 Hz) and recorded from

1144

the CA1 pyramidal cell soma maintained at a holding potential of -65 mV. **B**, Two-photon

1145

image of a dendritic segment (corresponding to the region shown by the red square in **A**)

1146

showing locations of glutamate uncaging (blue crosses). **C**, Amplitude of uEPSCs plotted

1147

against individual spine volume (open circles, n = 140 spines, 33 dendrites, 12 cells). Note

1148 that the uEPSC amplitudes recorded at the soma show a significant positive correlation with
 1149 the estimated spine volume. On average, four spines per dendrite were examined.

1150

1151

1152 **Figure 2-3: CA1 proximal stratum radiatum dendrites can be**
 1153 **grouped into two distinct populations based on the dendritic**
 1154 **diameter**

1155 Dendrites in the CA1 PSR can be grouped into two populations based on their dendritic
 1156 diameters. Dendrites with a diameter of less than 1 μm likely represent the oblique dendrites.
 1157 However, the large-diameter dendrites ($> 1.4 \mu\text{m}$) can either be the main apical shafts or the
 1158 segments of oblique dendrites near to the branch points.

1159

1160 **Figure 3-1: Spine density is positively correlated with the dendritic**
 1161 **diameter in the CA1 proximal stratum radiatum**

1162 Scatter plots of spine density against dendritic diameter in the CA1 PSR (**A**), cortex (**B**), and
 1163 CB (**C**). A significant positive correlation is detected between the spine density and the
 1164 dendritic diameter in the CA1 PSR.

1165

1166 **Figure 3-2: Neither the ratio of postsynaptic density area to neck**
 1167 **length, nor the average neck diameter correlates with the dendritic**
 1168 **diameter in the CA1 proximal stratum radiatum**

1169 Scatter plots show that neither the ratio of total PSD area to total neck length (**A**), nor the
 1170 average neck diameter (**B**) correlates with the dendritic diameter in the CA1 PSR.

1171

1172

1173

1174 **Figure 3-3: Synaptic constancy enables effective information**1175 **transfer from the dendrite to the soma**

1176 **A**, Schematic representation of a two-layer neuron model. A dendritic branch receives inputs
 1177 from 250 different synapses. Dendritic spikes from twenty branches were integrated at the
 1178 soma for somatic spiking. **B**, Case 1 shows that the synaptic strength in all the branches
 1179 obeys single lognormal distribution, and thus, the dendrites are of similar synaptic strength.
 1180 Case 2 shows that the synaptic strength in each branch obeys a lognormal distribution, but
 1181 the mean synaptic strengths (μ_e) differs across branches. The mean μ_e was chosen from the
 1182 Gaussian distribution $N(-6, 0.4)$. **C**, MI between the synaptic inputs and the occurrence of
 1183 dendritic spikes. The synaptic input from the strongest synapse was compared with the
 1184 characteristics of the resultant dendritic spike. **D**, MI between the synaptic inputs and
 1185 somatic spikes. In **(C)** and **(D)**, the left MI plots are based on the data from case 1, and the
 1186 right MI plots are based on the data from case 2.

1187

1188 **Figure 4-1: The amplitudes of uncaging-evoked excitatory**1189 **postsynaptic potentials negatively correlate with the spine neck**1190 **lengths**

1191 **A-B**, Plots of the uncaging potentials (peak amplitude) versus spine neck lengths. The same
 1192 plot in **A** is plotted in **B** by assigning a value of $0.2 \mu\text{m}$ to all the neck lengths shorter than
 1193 $0.2 \mu\text{m}$. The red circle indicates the average EPSPs of the spines whose neck lengths were

1194 shorter than 0.2 μm . **C**, Plot of the uncaging potentials (peak amplitude) versus head widths.

1195 Each circle in **A-C** represents dendritic spines ($n = 70$ spines, 22 dendrites, 6 cells). Lines

1196 are linear fit (Spearman's rank order test).

1197

1198 **Table 1: Frequency of filopodia, perforated spines, spinules, stubby spines and branched spines in**
1199 **different brain regions**

Brain region	Filopodia (%)	Perforated spines (%)	Spinules (%)	Stubby spines (%)	Branched spines (%)	Number of spines in branches (range)
CA1 PSR	1.78	2.72	3.26	2.90	7.97	2
CA1 SLM	0.00	50.00	8.57	1.43	0.00	— —
Cortex	3.07	8.60	0.90	2.26	9.50	2–4
Striatum	5.84	4.47	4.71	0.00	13.40	2–3
CB	4.19	0.00	0.61	0.00	12.62	2–5

1200

1201 Note: Filopodia lack synaptic contacts with the presynaptic terminals.

1202

1203

1204

1205

1206

1207

1208

1209

1210

Table 2: Dimensions of spine head and spine neck in different brain regions

Brain region	Spines Dendrites (n)	Spine density (mean \pm SD)	Head volume (mean \pm SD, ratio, CV)	Neck length (mean \pm SD, ratio, CV)	Neck diameter (mean \pm SD)	Ratio of PSD area to neck length (mean \pm SD)
CA1 PSR	552 23	3.04 \pm 0.825	0.05 \pm 0.045 124, 0.94	0.46 \pm 0.246 38, 0.54	0.20 \pm 0.087	0.19 \pm 0.193
CA1 SLM	70 12	0.75 \pm 0.360	0.12 \pm 0.086 35, 0.71	0.49 \pm 0.289 15, 0.59	0.25 \pm 0.127	0.32 \pm 0.323
CA3 PSR	8 ----	----	1.66 \pm 1.988 155, 1.20	----	----	----
Cortex	221 19	1.14 \pm 0.723	0.08 \pm 0.101 159, 1.26	1.09 \pm 0.561 20, 0.52	0.23 \pm 0.121	0.13 \pm 0.169
Striatum	403 21	1.94 \pm 0.621	0.07 \pm 0.109 204, 1.66	1.12 \pm 0.556 106, 0.50	0.26 \pm 0.104	0.11 \pm 0.204
CB	824 11	7.10 \pm 1.693	0.13 \pm 0.035 11, 0.27	0.74 \pm 0.300 27, 0.40	0.27 \pm 0.054	0.17 \pm 0.130

1211 Units: Spine density: spines/ μm , Head volume: μm^3 , Neck length: μm , Neck diameter: μm

1212 Note: Only the small diameter dendrites (diameter $< 1 \mu\text{m}$) are included for the spine density analysis in the CA1 PSR. Out of 23 dendrites
1213 analyzed, 16 dendrites fulfilled this criterion. All the spines, irrespective of the dendritic diameter of their parent dendrites, are included for head
1214 volume, neck length and neck diameter analysis.

1215 Ratio of head volume indicates the fold difference between the largest and smallest spine heads. Ratio of neck length indicates the fold
1216 difference between the longest and shortest spine necks. CV, coefficient of variation.

1217

1218

1219

1220

1221

1222

1223

1224

1225

1226

1227

1228

1229

1230

1231

1232

Table 3: PSD area unit dendritic length and the neck length unit dendritic length in different brain regions

Brain region	Dendritic diameter (mean \pm SD)	PSD area unit dendritic length (mean \pm SD)	Neck length unit dendritic length (mean \pm SD)	Ratio of total PSD area total neck length in dendrites (mean \pm SD)
CA1 PSR	0.59 \pm 0.104	0.18 \pm 0.055	1.35 \pm 0.442	0.14 \pm 0.018
CA1 SLM	0.58 \pm 0.097	0.08 \pm 0.031	0.37 \pm 0.268	0.27 \pm 0.112
Cortex	0.65 \pm 0.141	0.11 \pm 0.046	1.25 \pm 1.205	0.12 \pm 0.082
Striatum	0.77 \pm 0.096	0.15 \pm 0.057	2.16 \pm 0.906	0.08 \pm 0.029
CB	1.02 \pm 0.226	0.77 \pm 0.221	5.29 \pm 1.539	0.15 \pm 0.024

Units: Dendritic diameter: μm , PSD area unit dendritic length: μm , PSD area unit neck length: μm

Table 4: Frequency of axon-coupled spines in different brain regions

Brain region	Spines observed (n)	Axon-coupled spines (n)	Number of spines in a dendrite making synaptic contacts with the same axon (range)
CA1 PSR	552	26 (4.7%)	2
CA1 SLM	70	18 (25.7%)	2
Cortex	221	12 (5.4%)	2
Striatum	403	36 (8.9%)	2
CB	824	215 (26.1%)	2–4

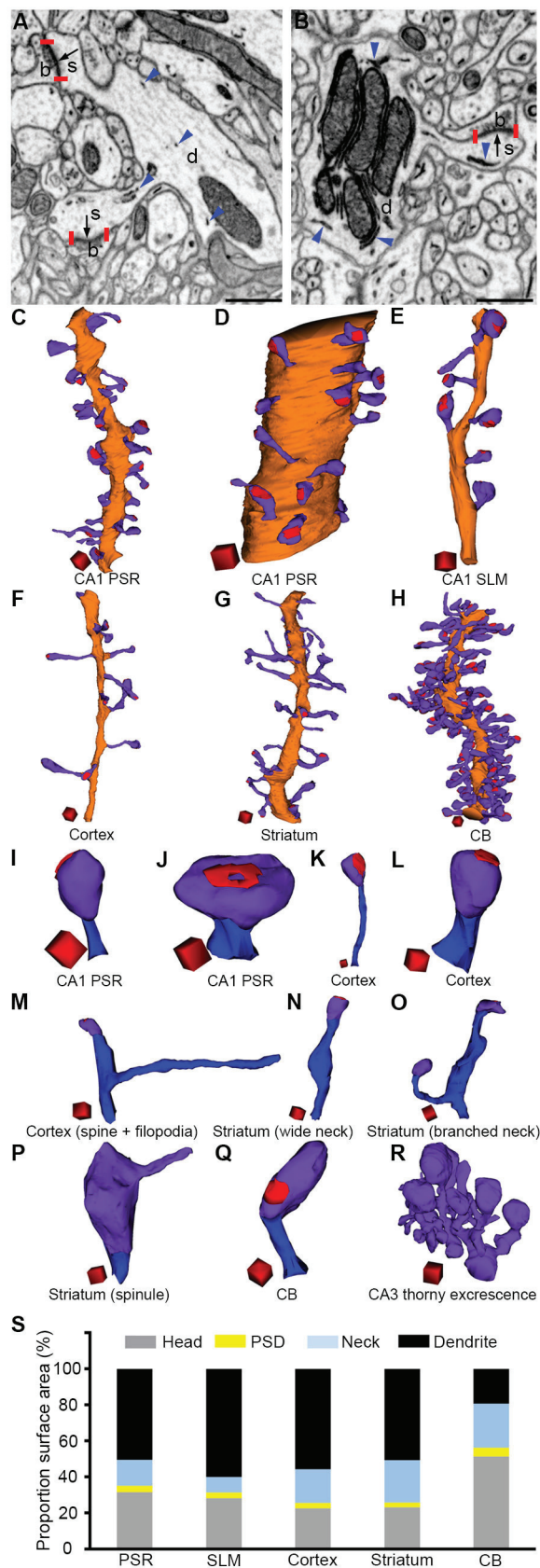
Note: Note that all the 824 spines studied in CB make synaptic contacts with the parallel fiber terminals.

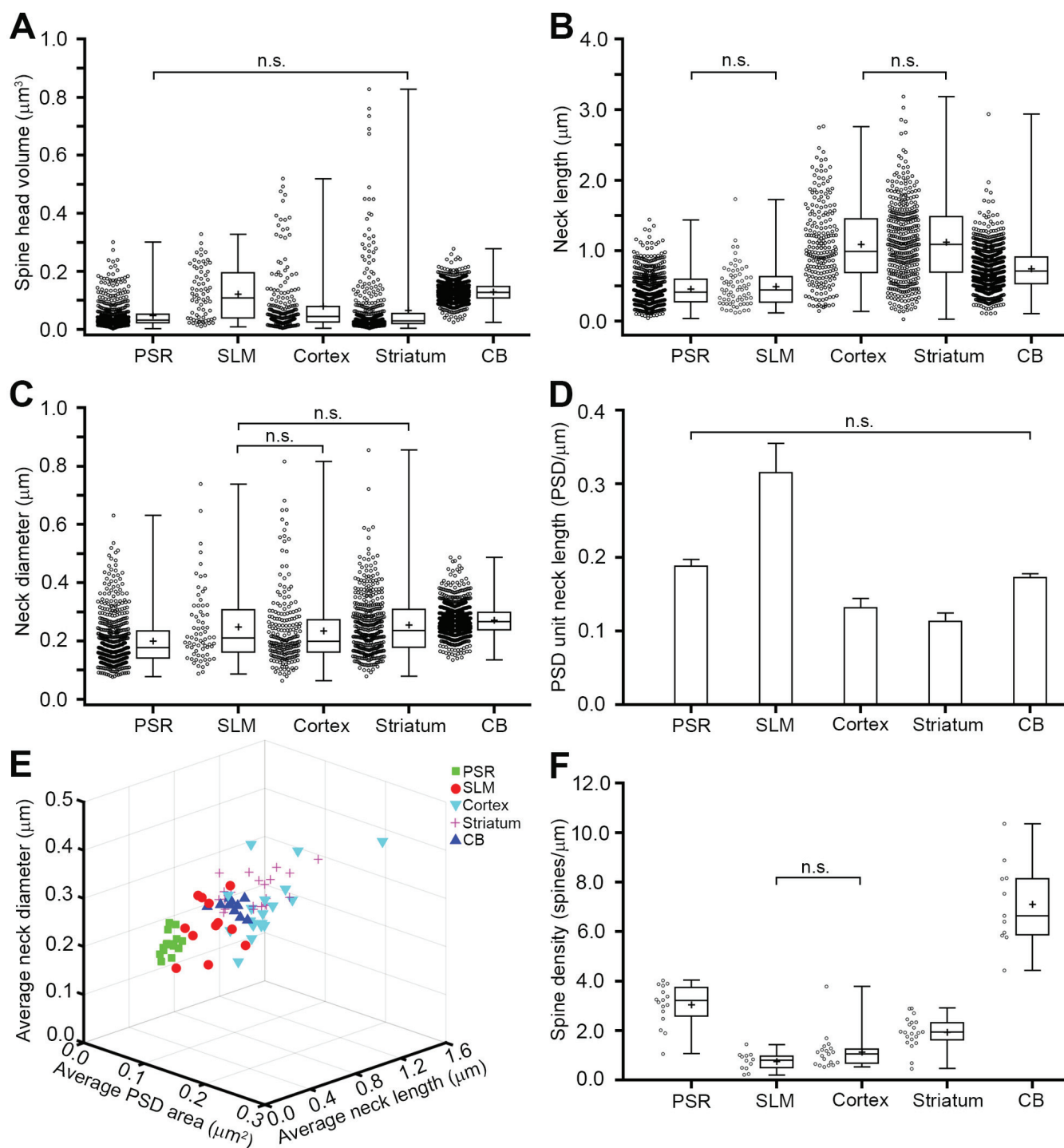
Table 5: Distribution of endoplasmic reticulum in spines

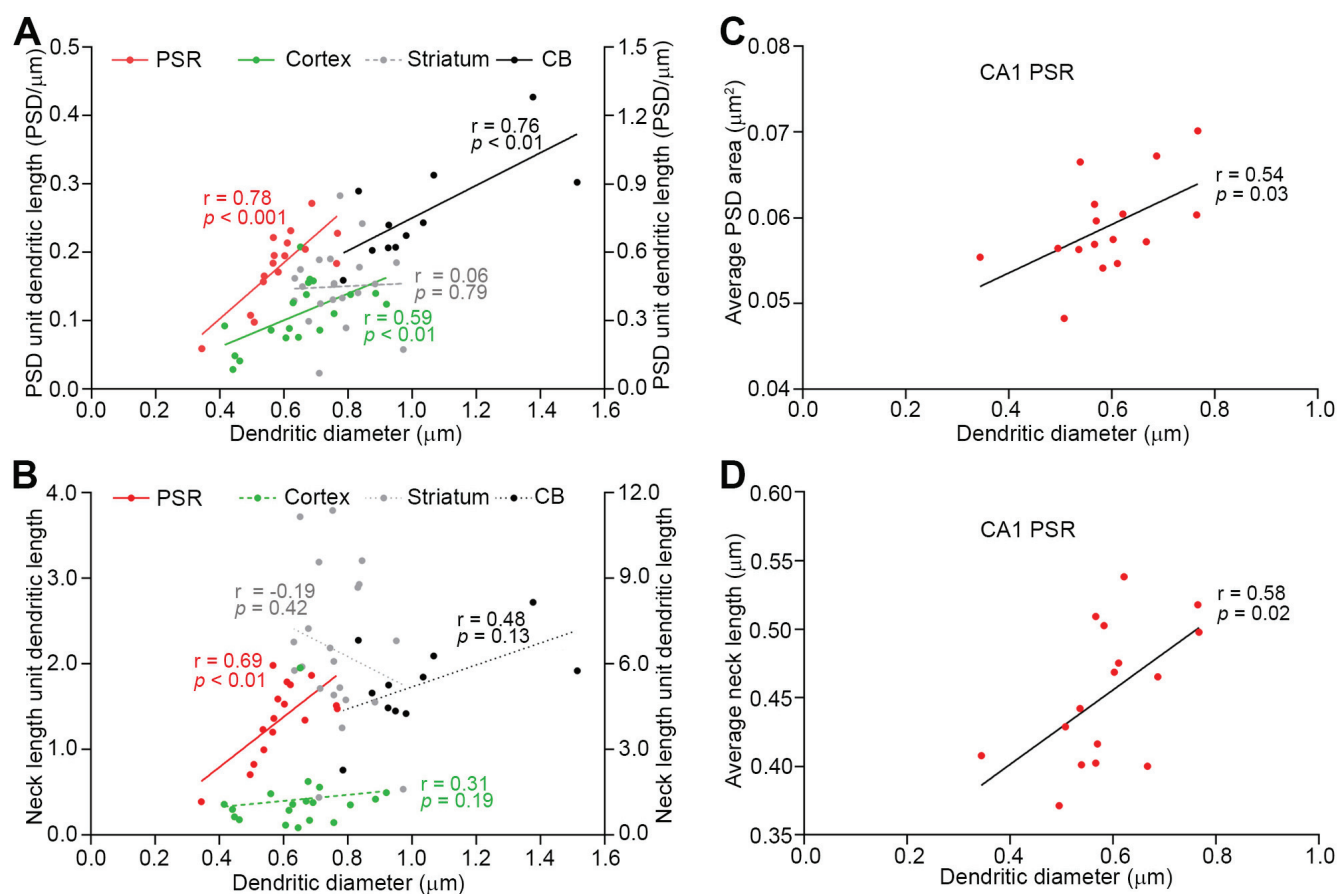
Brain region	Spines observed (n)	ER-containing spines (%)	Head volume (mean \pm SD)		Neck length (mean \pm SD)		Neck diameter (mean \pm SD)	
			ER+	ER-	ER+	ER-	ER+	ER-
CA1 PSR	552	13.6	0.11 \pm 0.073	0.04 \pm 0.030***	0.46 \pm 0.229	0.46 \pm 0.249	0.25 \pm 0.101	0.19 \pm 0.082***
CA1 SLM	70	15.7	0.18 \pm 0.077	0.11 \pm 0.084*	0.55 \pm 0.233	0.48 \pm 0.300	0.34 \pm 0.090	0.23 \pm 0.127**
Cortex	221	40.3	0.15 \pm 0.131	0.04 \pm 0.023***	1.03 \pm 0.566	1.13 \pm 0.557	0.30 \pm 0.143	0.19 \pm 0.075***
Striatum	403	55.1	0.10 \pm 0.137	0.02 \pm 0.017***	1.15 \pm 0.584	1.09 \pm 0.518	0.29 \pm 0.105	0.21 \pm 0.085***
CB	824	100	----	----	----	----	----	----

Units: Head volume: μm^3 , Neck length: μm , Neck diameter: μm

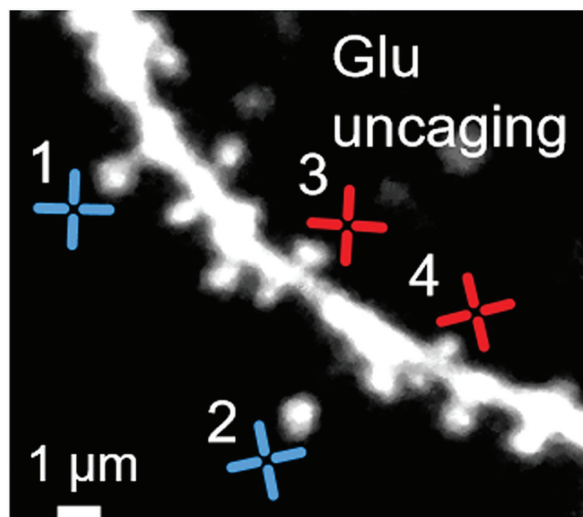
Note: Asterisks denote statistical significance in the dimensions of head volume and neck diameter between ER-containing (ER+) and ER-lacking spines (ER-) in each brain region.



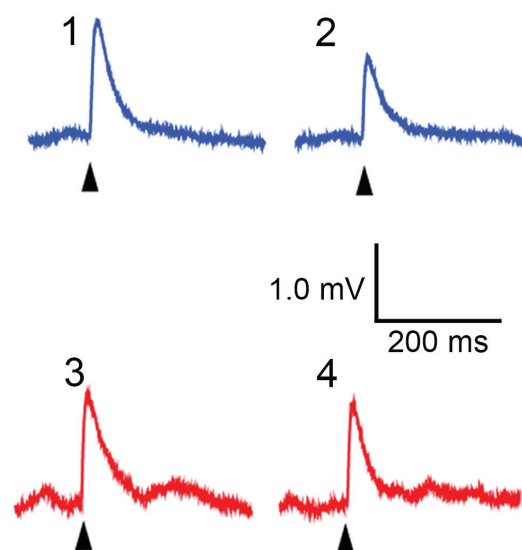




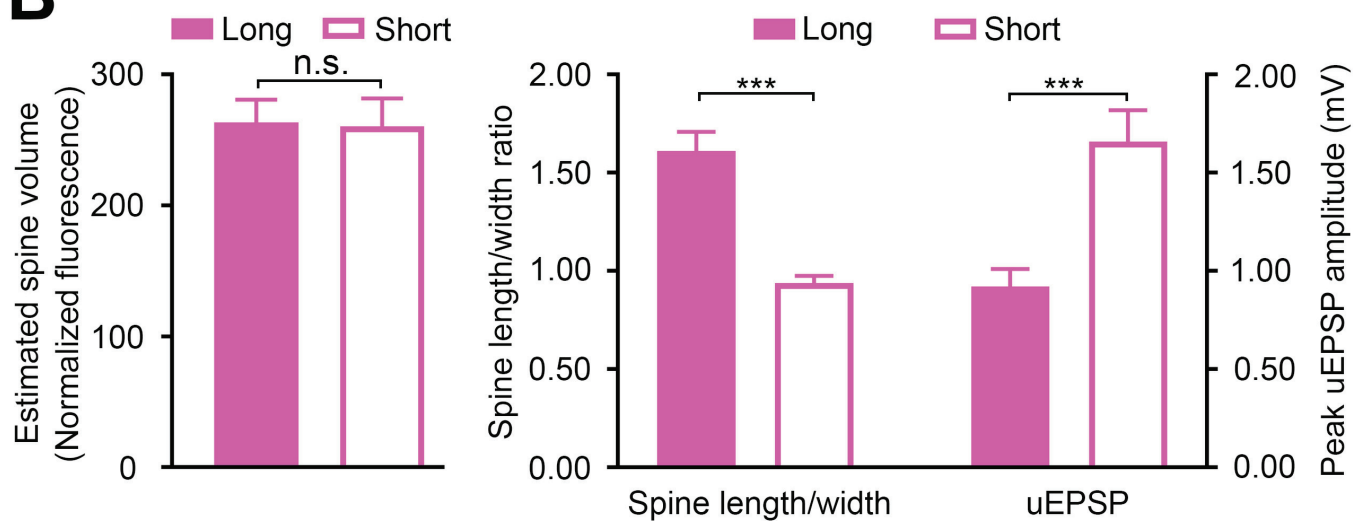
A

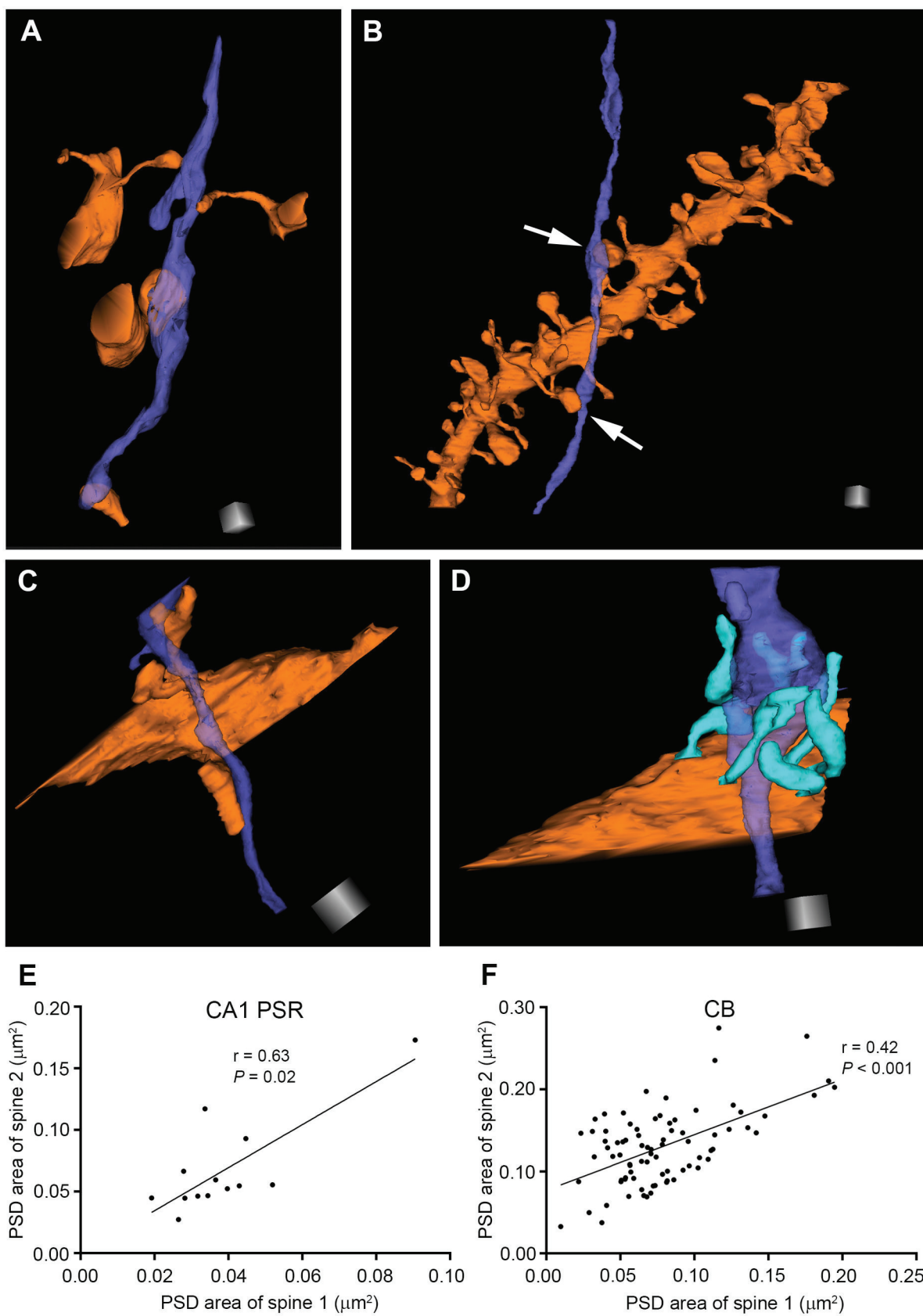


- + Similar head size, but different neck length
- + Different head size, but similar neck length



B





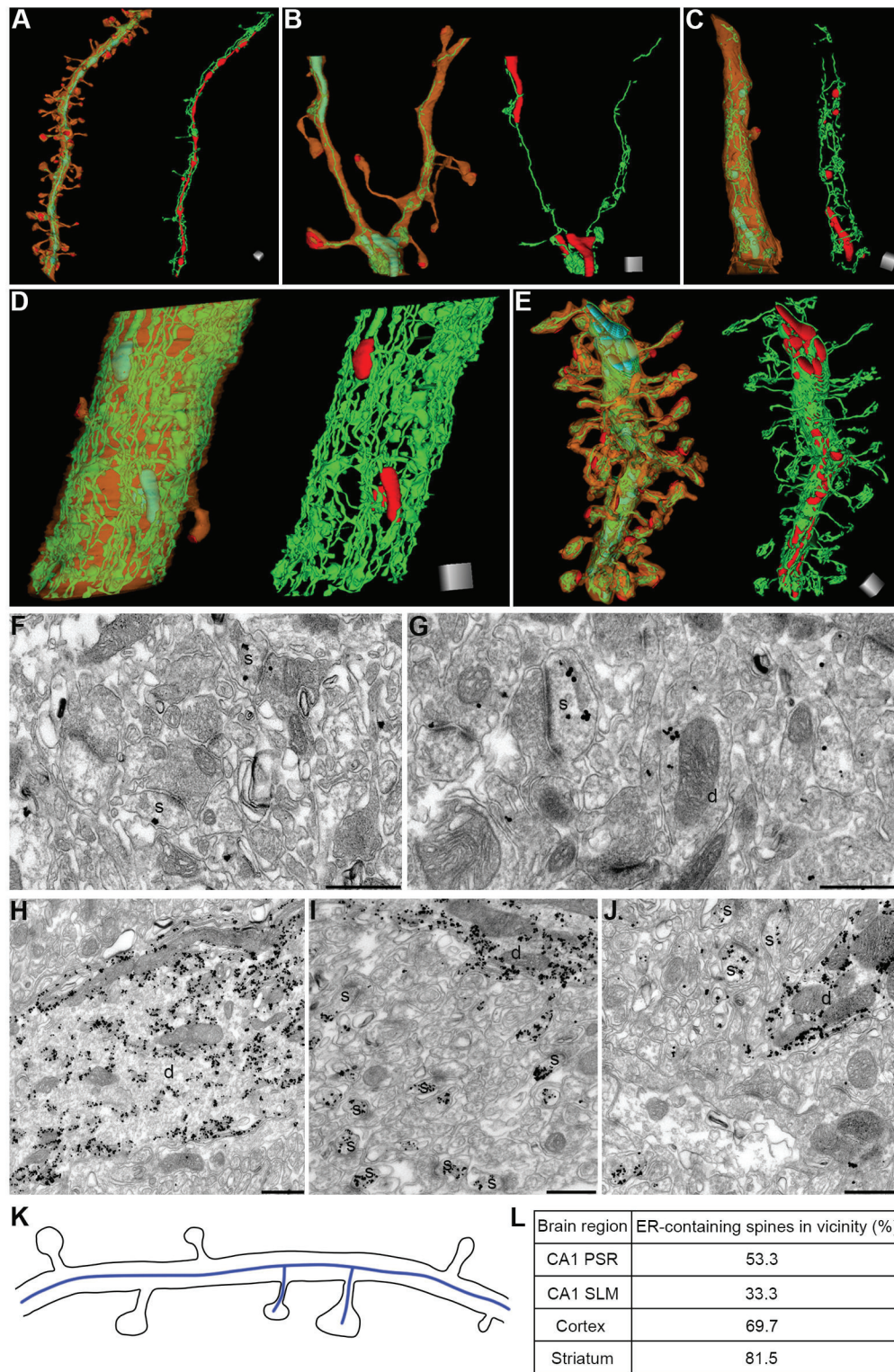


Table 1: Frequency of filopodia, perforated spines, spinules, stubby spines and branched spines in different brain regions

Brain region	Filopodia (%)	Perforated spines (%)	Spinules (%)	Stubby spines (%)	Branched spines (%)	Number of spines in branches (range)
CA1 PSR	1.78	2.72	3.26	2.90	7.97	2
CA1 SLM	0.00	50.00	8.57	1.43	0.00	--
Cortex	3.07	8.60	0.90	2.26	9.50	2–4
Striatum	5.84	4.47	4.71	0.00	13.40	2–3
CB	4.19	0.00	0.61	0.00	12.62	2–5

Note: Filopodia lack synaptic contacts with the presynaptic terminals.

Table 2: Dimensions of spine head and spine neck in different brain regions

Brain region	Spines Dendrites (n)	Spine density (mean \pm SD)	Head volume (mean \pm SD, ratio, CV)	Neck length (mean \pm SD, ratio, CV)	Neck diameter (mean \pm SD)	Ratio of PSD area to neck length (mean \pm SD)
CA1 PSR	552 23	3.04 \pm 0.825	0.05 \pm 0.045 124, 0.94	0.46 \pm 0.246 38, 0.54	0.20 \pm 0.087	0.19 \pm 0.193
CA1 SLM	70 12	0.75 \pm 0.360	0.12 \pm 0.086 35, 0.71	0.49 \pm 0.289 15, 0.59	0.25 \pm 0.127	0.32 \pm 0.323
CA3 PSR	8 ----	----	1.66 \pm 1.988 155, 1.20	----	----	----
Cortex	221 19	1.14 \pm 0.723	0.08 \pm 0.101 159, 1.26	1.09 \pm 0.561 20, 0.52	0.23 \pm 0.121	0.13 \pm 0.169
Striatum	403 21	1.94 \pm 0.621	0.07 \pm 0.109 204, 1.66	1.12 \pm 0.556 106, 0.50	0.26 \pm 0.104	0.11 \pm 0.204
CB	824 11	7.10 \pm 1.693	0.13 \pm 0.035 11, 0.27	0.74 \pm 0.300 27, 0.40	0.27 \pm 0.054	0.17 \pm 0.130

Units: Spine density: spines/ μm , Head volume: μm^3 , Neck length: μm , Neck diameter: μm

Note: Only the small diameter dendrites (diameter $< 1 \mu\text{m}$) are included for the spine density analysis in the CA1 PSR. Out of 23 dendrites analyzed, 16 dendrites fulfilled this criterion. All the spines, irrespective of the dendritic diameter of their parent dendrites, are included for head volume, neck length and neck diameter analysis.

Ratio of head volume indicates the fold difference between the largest and smallest spine heads. Ratio of neck length indicates the fold difference between the longest and shortest spine necks. CV, coefficient of variation.

Table 3: PSD area unit dendritic length and the neck length unit dendritic length in different brain regions

Brain region	Dendritic diameter (mean \pm SD)	PSD area unit dendritic length (mean \pm SD)	Neck length unit dendritic length (mean \pm SD)	Ratio of total PSD area total neck length in dendrites (mean \pm SD)
CA1 PSR	0.59 \pm 0.104	0.18 \pm 0.055	1.35 \pm 0.442	0.14 \pm 0.018
CA1 SLM	0.58 \pm 0.097	0.08 \pm 0.031	0.37 \pm 0.268	0.27 \pm 0.112
Cortex	0.65 \pm 0.141	0.11 \pm 0.046	1.25 \pm 1.205	0.12 \pm 0.082
Striatum	0.77 \pm 0.096	0.15 \pm 0.057	2.16 \pm 0.906	0.08 \pm 0.029
CB	1.02 \pm 0.226	0.77 \pm 0.221	5.29 \pm 1.539	0.15 \pm 0.024

Units: Dendritic diameter: μm , PSD area unit dendritic length: μm , PSD area unit neck length: μm

Table 4: Frequency of axon-coupled spines in different brain regions

Brain region	Spines observed (n)	Axon-coupled spines (n)	Number of spines in a dendrite making synaptic contacts with the same axon (range)
CA1 PSR	552	26 (4.7%)	2
CA1 SLM	70	18 (25.7%)	2
Cortex	221	12 (5.4%)	2
Striatum	403	36 (8.9%)	2
CB	824	215 (26.1%)	2–4

Note: Note that all the 824 spines studied in CB make synaptic contacts with the parallel fiber terminals.

Table 5: Distribution of endoplasmic reticulum in spines

Brain region	Spines observed (n)	ER-containing spines (%)	Head volume (mean \pm SD)		Neck length (mean \pm SD)		Neck diameter (mean \pm SD)	
			ER+	ER-	ER+	ER-	ER+	ER-
CA1 PSR	552	13.6	0.11 \pm 0.073	0.04 \pm 0.030***	0.46 \pm 0.229	0.46 \pm 0.249	0.25 \pm 0.101	0.19 \pm 0.082***
CA1 SLM	70	15.7	0.18 \pm 0.077	0.11 \pm 0.084*	0.55 \pm 0.233	0.48 \pm 0.300	0.34 \pm 0.090	0.23 \pm 0.127**
Cortex	221	40.3	0.15 \pm 0.131	0.04 \pm 0.023***	1.03 \pm 0.566	1.13 \pm 0.557	0.30 \pm 0.143	0.19 \pm 0.075***
Striatum	403	55.1	0.10 \pm 0.137	0.02 \pm 0.017***	1.15 \pm 0.584	1.09 \pm 0.518	0.29 \pm 0.105	0.21 \pm 0.085***
CB	824	100	----	----	----	----	----	----

Units: Head volume: μm^3 , Neck length: μm , Neck diameter: μm

Note: Asterisks denote statistical significance in the dimensions of head volume and neck diameter between ER-containing (ER+) and ER-lacking spines (ER-) in each brain region.